Towards a generalized imaging spectroscopy framework for surface soil salinity retrieval in coastal wetlands: Evaluating transferability and hydroperiod–salinity relationships

Daniel Jensen[1], Kyra Adams, [1] Antoine Soloy[1], Saoussen Belhadj-Aissa[1], Marc Simard[1], Connor Davis[1], Laven Naidoo[2,3], Pati Thakali[4], Elhadi Adam[4], Lara van Niekerk[5,6,7], Heidi van Deventer[3,7], Janine B. Adams[5,6,8], Ruth-Mary Fisher[9], Abigail Barrenblitt[10,11], Anthony Campbell[10,12]

[1]NASA Jet Propulsion Laboratory, California Institute of Technology, Pasadena, CA 91109
[2]Gauteng City-Region Observatory (GCRO), a Partnership of the University of Johannesburg, the University of the Witwatersrand, Johannesburg, the Gauteng Provincial Government and Organised Local Government in Gauteng (SALGA), Johannesburg, South Africa
[3]Department of Geography, Geoinformatics & Meteorology, University of Pretoria, Private Bag X20, Hatfield, Pretoria 0028, South Africa
[4]School of Geography, Archaeology and Environmental Studies, University of the Witwatersrand, Johannesburg 2050, South Africa
[5]Department of Botany, Nelson Mandela University, PO Box 77000, Gqeberha, South Africa, 6031
[6]Institute for Coastal and Marine Research, Nelson Mandela University, PO Box 77000, Gqeberha, South Africa, 6031
[7]Council for Scientific and Industrial Research (CSIR), PO Box 395, Pretoria 0001, Stellenbosch 7600, South Africa
[8]DSI/NRF Research Chair: Shallow Water Ecosystems, Nelson Mandela University, PO Box 77000, Gqeberha, South Africa, 6031
[9]Cape Research Centre, South African National Parks, Tokai, 7945, South Africa.
[10]NASA Goddard Space Flight Center, Greenbelt, Maryland, USA.
[11]Earth System Science Interdisciplinary Center, University of Maryland, College Park, Maryland, USA
[12]Goddard Earth Sciences Technology and Research (GESTAR) II, University of Maryland, Baltimore County, Baltimore, Maryland, USA

Key Points

- Airborne imaging spectrometer data collected over coastal wetlands in California and South Africa were applied to map soil salinity.
- The soil salinity model was trained with reflectance data collected in California and validated at each site to test transferability.
- Opposing hydroperiod–salinity relationships reflect contrasting inundation and hydrologic connectivity between the two wetlands.

Abstract

Coastal wetlands are threatened by changing climatic and hydrologic pressures that may salinize fresh-brackish ecosystems, causing stress, transformation, or collapse. Monitoring soil salinity requires a generalizable remote sensing approach applicable across coastal environments. We collected *in situ* field spectrometer reflectance measurements and soil samples in California's Carpinteria Salt Marsh Reserve (CSMR) to measure salt content. The first derivatives of these reflectances were used in a Partial Least Squares Regression (PLSR) model to predict soil salinity (n = 32, R^2 = 0.90, Mean Absolute Error (MAE) = 5.00 ppt). We applied the model to NASA's AVIRIS-3 imaging spectroscopy data to map soil salinity in the CSMR (Validation: n = 32, R^2 = 0.53, MAE = 9.22 ppt) and to AVIRIS-NG data over South Africa's Langebaan Lagoon to test model transferability (Validation: n = 11, R^2 = 0.67, MAE = 14.11 ppt). Primary mapped retrievals and associated analyses were restricted to non-submerged, soil-dominated pixels with MESMA-derived soil fractional cover ≥0.50. Reported retrieval performance therefore applies primarily to areas with substantial exposed soil. We used Sentinel-1 Synthetic Aperture Radar time series to map hydroperiod—the percentage of time a site was inundated over the data record—for comparison with the soil salinity maps. Soil salinity increased with hydroperiod at CSMR but decreased with hydroperiod at Langebaan Lagoon, consistent with differing hydrologic connectivity and inundation dynamics. These results demonstrate the potential for a transferable imaging spectroscopy framework for mapping surface soil salinity in coastal wetlands and for quantifying landscape-scale hydro-ecological controls on salinity patterns.

Plain Language Summary

Monitoring changes in salinity in coastal environments is a critical capability for assessing ongoing threats from changing climatic and hydrologic patterns such as sea level rise. There is a need for a generalizable remote sensing approach to estimate soil salinity across coastal wetlands without the need for site-specific studies. In April 2024, we collected reflectance measurements paired with soil samples in California's Carpinteria Salt Marsh Reserve (CSMR), with which we developed a predictive model for estimating soil salinity. The reflectance measurements capture the spectral characteristics of salt deposits within the soil samples, and we used the resulting model to map soil salinity across the CSMR using data captured by NASA's AVIRIS-3 instrument. To test the potential for applying our approach across different sites, we applied the model to AVIRIS-NG data collected over South Africa's Langebaan Lagoon. We then examined the relationship between each site's hydrologic drivers and our derived soil salinity. Our analysis demonstrates imaging spectroscopy's capability for mapping soil salinity in sparsely vegetated areas and the potential for a generalized algorithm.

Keywords

AVIRIS, BioSCape, Coastal Wetlands, Hydrology, Hyperspectral, Imaging Spectroscopy, Sentinel-1, Soil Salinity

1. Introduction

Coastal marshes are critical regions of ecological and human activity (Martínez et al., 2014; Michael et al., 2017). Being the terminal terrestrial landscapes that encompass the habitat gradient between fresh and saline systems, coastal marshes provide numerous essential functions that benefit both the environment and human communities (Day et al., 2024). These include acting as natural buffers against storms, providing vital habitats for diverse wildlife, and providing fertile soil for agricultural activities where salinity is low (FitzGerald et al., 2008). Additionally, wetlands support many biogeochemical cycles driven by fresh-saline water interactions, and play an essential role in nutrient cycling and water quality control to the nearshore system (Snedden et al. 2014; Day et al., 2024).

These highly dynamic coastal landscapes are under threat, with pressures coming from both oceanic and terrestrial drivers (Michael et al., 2017; Adams et al., 2024). On the ocean side, changing patterns in sea level and episodic storms force saline water further inland (Adhikari et al., 2019; Hamlington et al., 2020; IPCC, 2021), salinizing previously fresh to brackish regions and thereby degrading wetlands or causing their collapse through saltwater intrusion (Adams et al., 2024). On the landward side, changing recharge patterns, land use, and irrigation practices can alter freshwater hydrology, leading to unintended consequences such as exacerbated saltwater intrusion due to lowered groundwater or bottom-up groundwater flooding (White and Kaplan, 2021). Freshwater inflow obstruction causes desiccation and salinization, particularly of supratidal salt marshes in estuaries (Adams, 2020). Together, these hydrological pressures disrupt the delicate balance of fresh and saline waters in coastal wetlands, leading to negative impacts such as vegetation dieback, biodiversity loss, habitat degradation, increased erosion, and further diminished regional capacity for natural flood protection (Baldwin and Mendelssohn, 1998;

105 Lorrain-Soligon et al., 2023). Despite the protected status of many coastal habitats, interactions
106 among seawater, groundwater, and freshwater can extend beyond reserves and degrade the
107 ecological condition of the habitats and species. Monitoring changes in salinity is therefore
108 critical.

109 The interactions between fresh surface water, fresh groundwater, and saline seawater are
110 spatially variable and highly dynamic in time due to sporadic groundwater recharge—varying
111 with local rainfall, geology, and hydrology patterns—and variable ocean forcing (Michael et al.,
112 2003; Heiss and Michael, 2014; Kim et al., 2017). Due to the steep salinity and chemical
113 gradients between the surface and subsurface waters, these interactions drive many
114 biogeochemical reactions within coastal systems. This is especially critical in moderating the
115 nutrient cycling in organic-rich wetland environments, where salt content can alter microbial
116 nutrient transformations and constrain plant nutrient uptake (Ullman et al., 2003; Kim et al.,
117 2017 & 2019). Further, many coastal regions also host various human activities including
118 agricultural fields, which can further exacerbate saltwater intrusion via freshwater pumping and
119 irrigation, creating complex patterns of soil salinity in coastal areas (Gopalakrishnan et al.,
120 2019). While salinity can refer to salt dissolved in open water or groundwater, here we examine
121 soil salinity, that is the salt content that is either crystallized on or dissolved within the water of
122 surficial soils. In this context, salinity reflects the combined influence of marine inundation,
123 freshwater inputs, and evapoconcentration, making it a useful indicator of coastal wetland
124 hydrology and potential ecosystem degradation or marsh collapse.

125 Despite soil salinity's critical role in the overall health of coastal wetland systems, most
126 salinity monitoring efforts in these environments focus on point-measurements of water salinity
127 (Shahrayini and Noroozi, 2022; Zhu et al., 2021; George and Kumar, 2015). Episodic inundation

from storms or high tides can quickly change soil salinity levels. Underlying hydrologic patterns such as groundwater depletion and subsurface saltwater intrusion can also salinize different regions of coastal ecosystems. However, recovery to equilibrium conditions critical for ecosystem health can be slow and difficult, and may require decades (Yang et al., 2022). Remediation efforts—e.g., managed freshwater flushing, fixing drainage pathways, or soil amendment—need to be quickly deployed for maximum efficiency and chance of success. In-field soil salinity assessment methods exist, but are often limited by access, cost, and temporal consistency for monitoring and remediation efforts. Remote sensing has the potential to address these shortcomings with landscape and regional-scale data and is capable of quantifying and mapping soil characteristics (Kim et al., 2012; Forkuor et al., 2017). While soil salinity occupies a crucial role in directly understanding expected plant health, ecosystem dynamics, and the success of restoration efforts, no generalized method currently exists to map and monitor soil surface salinity at large scales and across different coastal environments.

Other studies have modelled and mapped soil salinity using remote sensing data, though most published studies are primarily concerned with estimating soil salinity in agricultural areas. Many of these studies employ multispectral data, e.g., from Landsat 8 Operational Land Imager (OLI) at a 30 m spatial resolution (Habibi et al., 2021; Shahrayini and Noroozi et al., 2022) or the Moderate Resolution Imaging Spectroradiometer (MODIS) with spatial resolutions from 250 m to 500 m and 1 km (Nguyen et al., 2024), to model soil salinity as measured by electrical conductivity (EC) based on numerous broad reflectance bands and their derived indices. Broad bands and indices from multispectral instruments may detect spectral relationships caused indirectly by salinity levels, but they do not capture the full potential of a salt's associated spectral characteristics that may be detectable in a visible-shortwave infrared (VSWIR)

reflectance spectrum. Airborne and spaceborne imaging spectrometers that measure spectral responses across hundreds of contiguous narrow bands have the potential to accurately quantify these spectral characteristics (Yu et al., 2020). There have been a handful of studies that investigated imaging spectroscopy for soil salinity. For example, George and Kumar (2015) applied Hyperion data with a machine learning classification approach to predict salinity severity classes across an alluvial plain based on selected indices. Another recent study (Das et al., 2023) used a machine learning regression approach with the Airborne Visible/Infrared Imaging Spectrometer-Next Generation (AVIRIS-NG) data in an Indian cropland area to predict soil EC and to develop a "hyperspectral soil salinity index (HSSI)". Silva et al. (2025) employed AVIRIS-NG to estimate and map soil salinity in a Southern California tidal wetland. This was done using a machine learning regression model trained on a selection of spectral indices and elevation. In doing so, the authors use the spectral characteristics of vegetation and the hydrogeomorphic constraint of elevation to infer the underlying soil salinity in a particular study area. These existing studies that estimate soil salinity, generally via EC, are focused on agricultural regions and rely on fully exposed soil for model applications or infer salinity from vegetation characteristics. This can be done when fields are bare or through a model framework, but the approaches outlined in current literature are not conducive to retrievals of salt concentrations in environments where observed spectra result from the mixture of soil, water, and different vegetation types.

This study aims to develop a generalized imaging-spectroscopy framework for mapping soil salinity in coastal wetlands using the surface soil's (top 2 cm) observable spectral characteristics. Our primary goal is to train and develop a soil salinity retrieval model for coastal wetlands using *in situ* and airborne spectroscopy data, and to subsequently test the model's

transferability with a different region serving as an independent validation site. We thus use *in situ* soil samples and reflectance data collected in a coastal salt marsh in California, USA, to train the model, and coincident airborne imaging spectrometer data to apply the model. We hypothesize that the model exploits spectral structure associated with salt-affected soil surfaces and that this retrieval is transferable across sites to a useful degree despite differences in substrate, moisture conditions, and vegetation. We then test the generalizability of our approach by applying our model to imagery and field data collected in the Langebaan Lagoon in South Africa's Western Cape Province. With soil salinity maps in these two study areas, we then investigate our secondary goal of assessing the impact of hydrology on salinity distributions. We hypothesize that hydroperiod—the percent of time a wetland area spends inundated as derived from spaceborne synthetic aperture radar (SAR)—has a significant relationship to the distribution of soil salinity which, in turn, is dependent on each site's unique hydrology. Together, our analyses test both the feasibility of developing a transferable surface soil salinity retrieval algorithm using imaging spectroscopy and our approach's utility for investigating hydro-ecological controls of soil salinity in complex coastal wetland environments.

2. Methods

To test the feasibility of retrieving soil salinity in coastal wetlands, we explored two different wetland sites, one in California (Carpinteria Salt Marsh Reserve; CSMR) and one in South Africa (Langebaan Lagoon) (Figure 1). The CSMR is located adjacent to the city of Carpinteria and is characterized by both natural and artificial channels that drain the southern slopes of the nearby Santa Ynez Mountains. The marsh is characterized by a mixed semidiurnal tidal regime set within a Mediterranean climate with warm dry summers and mild, moist winters (Carpinteria Salt Marsh Reserve Management Plan, 2026). At the CSMR, we collected field data

coincident with an AVIRIS-3 flight on April 16, 2024. The Langebaan Lagoon is a micro-tidal environment that stretches 15 km parallel to the coastline, occupying a temperate region of South Africa also with dry and warm summers (Flemming 1988). The main source of freshwater is through diffuse groundwater discharge from the Elandsfontein and Langebaan Road Aquifers (Israel et al., 2021). The lagoon was declared a Ramsar site—a wetland designated to be of international importance—in April 1988 (Convention on Wetlands (Ramsar), 1991). In the CSMR, we collected field and airborne imaging spectroscopy data to train and test our soil salinity retrieval algorithm. Salinity here is defined as the total amount of dissolved solids in water in parts per thousand by weight (Hale and Margham, 1988). At the Langebaan Lagoon in South Africa, we leveraged AVIRIS-NG flights and field data collected for the BioSCape campaign in October of 2023 (Figure 1). We used the in situ data collected at the CSMR to calibrate our soil salinity retrieval model and assess the model's applicability to coincidentally collected airborne imaging spectrometer data. We then applied our calibrated model to imaging spectrometer and additional field data collected at the Langebaan Lagoon to perform an independent validation of our soil salinity retrieval approach and to assess its transferability.

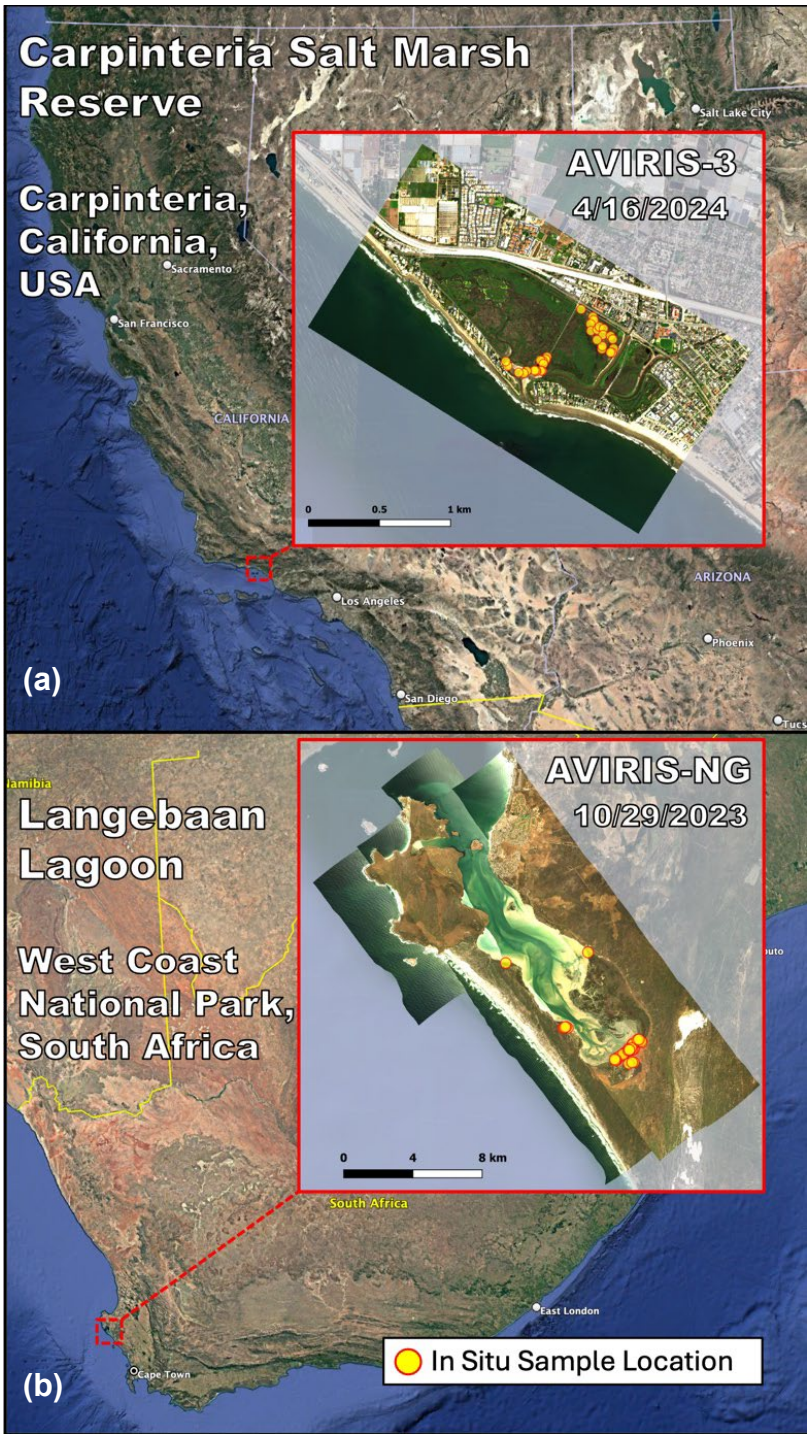


Figure 1: Study areas showing red-green-blue band composite images of **(a)** the AVIRIS-3 data collected over the Carpinteria Salt Marsh Reserve in California, USA, and **(b)** the AVIRIS-NG data collected over the Langebaan Lagoon in South Africa's West Coast National Park. Field sample locations are also indicated for each site. Dates indicate when each airborne dataset was collected. The AVIRIS-3 data was collected at 18:50 UTC on April 16, 2024, when the local tide level was 0.841 m below Mean Sea Level (MSL). The AVIRIS-NG data began collection at 09:49 UTC on October 29, 2023, when the local tide level was 0.077 m above MSL.

220 *2.1. Data*

221 *2.1.1. Airborne Imaging Spectrometer Data*

222 The AVIRIS-3 instrument was flown over the CSMR at approximately 12,500 ft (3,810
223 m) on April 16, 2024, collecting a single image spanning the marsh. AVIRIS-3, flown onboard
224 Dynamic Aviation's B-200 King-Air platform, has a 40-degree instantaneous field of view with
225 1234 cross-track pixels, providing a ground sampling distance (or pixel resolution) of 2.1 meters
226 for this image. AVIRIS-3 is a copy of the Dyson imaging spectrometer used by the Earth Surface
227 Mineral Dust Source Investigation (EMIT) instrument that has been deployed on the
228 International Space Station, measuring surface and atmospheric radiances with 284 bands in the
229 wavelength range from 390 nm to 2500 nm with 7.4 nm sampling (Green, 2022). For this study
230 the L1B at-sensor radiance product (Eckert et al., 2024) was processed to L2A surface
231 reflectance (Brodrick et al., 2025) using an optimal estimation (OE) based atmospheric
232 correction procedure, fully described in the EMIT Level 2A Algorithm Theoretical Basis
233 Document (ATBD; Thompson et al., 2020). The OE algorithm calculates the surface reflectance
234 and associated uncertainty for each pixel, together defining the posterior probability of the
235 surface reflectance given the at-sensor radiance measurement.

236 AVIRIS-NG, AVIRIS-3's predecessor instrument, was flown over the Langebaan Lagoon
237 on October 29, 2023 onboard the National Aeronautics and Space Administration's (NASA) GIII
238 platform in South Africa's Greater Cape Floristic Region as part of the BioSCape project. The
239 GIII aircraft flew at roughly 21,000 ft (6,400 m), collecting data with a 6.3 m spatial resolution.
240 AVIRIS-NG measures radiance at 5-nm intervals across 425 bands from 380-2510 nm. The L1B
241 at-sensor radiance products generated from the BioSCape collection were atmospherically

corrected with OE algorithm, as with AVIRIS-3, to generate this study's surface reflectance data (Brodrick et al., 2026).

2.1.2. In Situ Data: Soil Samples and Field Spectroscopy

At the CSMR, field measurements of soil reflectance were taken with an Analytical Spectral Devices (ASD) Field Spec-3 spectrometer, collecting data with 1 nm sampling from 350 to 2500 nm, coincident with the AVIRIS-3 overflight. We concurrently collected 32 *in situ* soil samples from the top 2 cm of exposed soil locations. Sampling locations were selected to span the range of exposed-soil surface conditions observed during the overflight, including variability in apparent mineralogic composition and surface organic material/biofilm, to ensure the model was trained across realistic within-marsh surface heterogeneity rather than tuned to a single surface state. After collection, the CSMR soil samples were analyzed in the laboratory to characterize the soil and accurately measure the samples' total salt content. Each sample was subsampled (~50 g) using a precision scale (0.1 g accuracy) and transferred into an aluminum tray. The samples were then left under a heating lamp for one week to remove moisture. After drying, the samples were weighed again to determine water content by comparing pre- and post-drying mass. For salinity analysis, the dried soil samples were mixed with a fixed volume (100 mL) of distilled water and agitated for 10 minutes to extract soluble salts. Electrical conductivity (EC) was measured using an EC-3185 Waterproof Soil EC/Total Dissolved Solids (TDS)/Conductivity Tester, which has a conductivity range of 0.00–19.99 mS/cm, a resolution of 0.01 mS/cm, and an accuracy of ±2% of the full scale. The device was manually calibrated before measurements to reflect an EC of 0 in the pure distilled water. Automatic temperature compensation was applied, and the solution temperatures at the time of measurement were recorded.

The measured EC values were converted into total salt mass using Equation 1:

$$m_{total\ salt} = (EC \times F) \times \frac{m_{water}}{1000} \quad (1)$$

where $m_{total\ salt}$ is the absolute mass of salt in grams, EC is the solution conductivity in milli-Siemens per centimeter, F is the conversion factor to convert conductivity into grams of salt per liter of solution ($F = 0.6$ g/L per mS/cm), and m_{water} is the added mass of distilled water in grams ($m_{water} = 100$g). Soil salinity measurement followed standard electrical conductivity protocols adapted from U.S. Salinity Laboratory Staff (1954) and Rhoades et al. (1999), using a dilute soil-water extraction method (approximately 1:2 mass ratio) with 10 minutes agitation to ensure complete dissolution of water-soluble salts (Bado et al., 2016; Herrero and Castañeda, 2015). All EC measurements were standardized to 25°C using the temperature correction equation (Equation 4) based on the 2% per degree Celsius coefficient provided in Table 15 of the United States Department of Agriculture (USDA) Handbook 60 (U.S. Salinity Laboratory Staff, 1954), which accounts for the temperature-dependent mobility of ions in solution. The conversion factor (F = 0.6 g/L per mS/cm) to convert conductivity to total salt concentration was adopted from the Department of Primary Industries and Regional Development (2022) and applied to the specific volume of water added (100 mL) using Equation 1 to calculate the absolute mass of salt in each sample.

This dilute extraction approach was selected to quantify total water-soluble salt mass in small surface samples for spectral model calibration. The approximately 1:2 soil-to-water mass ratio ensured complete dissolution of soluble salts while maintaining sufficient solution concentration for accurate EC measurement within the instrument's operational range. Such approaches are commonly applied in studies focused on relative salt content and remote sensing calibration, where consistency and complete extraction of soluble salts are prioritized over

standardized agronomic reporting units (Rhoades et al., 1999; Herrero and Castañeda, 2015). Because our retrieval model is trained on reflectance features sensitive to total surface salt content, consistent quantification of absolute salt mass was essential.

The resulting total salt mass was normalized by both the wet soil mass ($m_{wet\ sample}$, eq 2) and dry soil mass ($m_{dry\ sample}$, eq 3) to compute two distinct salinity metrics: S_{wet}, the wet soil relative salinity (g of salt per g of wet soil), which reflects field moisture conditions, and S_{dry}, dry soil relative salinity (g of salt per g of dry soil), which provides a standardized measure for inter-sample comparison that can be converted to parts per thousand (ppt).

$$S_{wet} = \frac{m_{total\ salt}}{m_{wet\ sample}} \tag{2}$$

$$S_{dry} = \frac{m_{total\ salt}}{m_{dry\ sample}} \tag{3}$$

The descriptive statistics from the resulting dry relative soil salinity values, along with sample water content, are reported in Table 1. Field soil samples exhibited substantial variability in our calibration dataset from the Carpinteria Salt Marsh Reserve (n = 32) for both sample dry relative salinity and the water content. This variability provided sufficient dynamic range for training and evaluating the salinity retrieval model.

In the Langebaan Lagoon site, our independent validation dataset for testing model transferability (n = 19) consisted of two sets of *in situ* salinity measurements collected November 5-10, 2023: 11 measurements of extracted porewater from vegetation survey plots using either a salinometer or refractometer, using porewater salinity as a proxy for soil salinity; and 8 direct measurements of soil EC (mS/cm), again using a EC-3185 Waterproof Soil EC/TDS/Conductivity Tester. Note that samples from the EC-3185 that measured at the saturation value of 19.99 mS/cm were discarded due to their inability to accurately estimate

salinity. Porewater salinity and probe-based soil EC are related but non-equivalent measures: the former reflects dissolved salts in extracted water, whereas the latter is also influenced by soil moisture, texture, and temperature. We therefore treat them as complementary proxies for local soil salinity, while acknowledging that methodological differences may contribute to disagreement with remotely sensed estimates. Each *in situ* EC measurement included a concurrent soil temperature (°C) measurement. We converted the EC measurements to ppt by applying the conversion factor of 0.6 (Equation 1) after correcting each EC measurement for temperature to a 25° Celsius standard with Equation 4:

$$\widehat{EC} = \frac{EC}{1 + (0.02 \times (Temperature - 25))} \quad (4)$$

Table 1: *In situ* soil sample descriptive statistics

	Carpinteria Salt Marsh Reserve	Langebaan Lagoon
n	32	19
Mean Relative Salinity (ppt) ± Standard Deviation	24.66 ± 18.49	38.07 ± 23.66
Relative Salinity Range (ppt)	0.41-60.94	4.65-94.93
Mean Water Content (%) ± Standard Deviation	16.74 ± 7.46	-
Water Content Range (%)	0.00-30.41	-

*For the Carpinteria Salt Marsh Reserve the Mean Relative Salinity values are derived from the sample dry relative salinity measurements. For the Langebaan Lagoon data, these are derived from both soil EC probe and refractometer measurements of porewater salinity. Soil water content was not measured in the Langebaan Lagoon.

2.2. Partial Least Squares Regression

With the soil salinity calculated for each sample from the CSMR, we paired the lab-measured salinity values with their corresponding *in situ* reflectance data. The 1nm reflectance samples were resampled to the 7.4 nm spectral resolution of AVIRIS-3, as well as to the 5nm

326 spectral resolution of AVIRIS-NG. For each AVIRIS dataset, the *in situ* reflectance spectra were
327 convolved to match the respective set of bands using Gaussian functions as defined by the Full
328 Width at Half-Maximum (FWHM) values reported in the image header files. Each 1-nm
329 reflectance value from the *in situ* spectra that fell within the corresponding 7.4 or 5 nm AVIRIS
330 band was input into the Gaussian function, with the output values then normalized by dividing by
331 the sum of their absolute values. The normalized output and observed reflectance matrices were
332 multiplied to return each simulated AVIRIS-3 or AVIRIS-NG reflectance band.
333 We then trained Partial Least Squares (PLS) Regression (PLSR) models using all *in situ*
334 data samples such that the first derivative of those convolved *in situ* reflectances were the
335 independent variables and the corresponding dry soil relative salinity values formed the
336 dependent variable. We first removed bands in the ranges of 1320-1500 and 1780-2055 nm
337 wavelengths due to atmospheric water vapor interference, leaving 245 AVIRIS-3 bands and 300
338 AVIRIS-NG bands, respectively. We determined the optimal number of PLS components (or
339 latent variables) for the model by calculating the Predicted Residual Sum of Squares (PRESS; g
340 salt per g of dry soil) for the range of one to fifteen components. This calculation used a Leave-
341 One-Out Cross Validation (LOOCV) wherein the model with the minimum summed value
342 indicates the optimal number of components. Based on the 245 input derivative bands, the
343 optimal PLSR model employed six components. Using the first derivative of reflectance in the
344 PLSR makes the model more sensitive to spectral slope and absorption features in the spectra
345 (Byrd et al., 2014; Jensen et al., 2019), including those that align with NaCl's spectral
346 characteristics (Li et al., 2015). With this PLSR model trained on the *in situ* salinity and
347 reflectance data from the CSMR, we can then assess its performance when applied to the

coincident AVIRIS-3 data collected over the CSMR and its transferability with the AVIRIS-NG data and independent salinity field samples in South Africa's Langebaan Lagoon.

2.3. Airborne Imaging Spectrometer Data: Processing and Mapping Soil Salinity

To apply the model to the AVIRIS-3 and AVIRIS-NG data, we identified suitably exposed soil pixels using Multiple Endmember Spectral Mixture Analysis (MESMA). Based on the EMIT MESMA implementation (Brodrick, 2024) and spectral library of *in situ* reflectances collected (Ochoa et al., 2025) with added soil reflectance spectra from the field spectrometer deployed in the CSMR, this provided per-pixel fractional cover estimates of non-photosynthetic vegetation (NPV; 34 endmember samples), green vegetation (GV; 48 endmember samples), and soil (124 endmember samples) for the CSMR and Langebaan Lagoon study sites (Figure 2). 92 of the soil reflectance samples used in our MESMA implementation were from the EMIT spectral library (Brodrick, 2024; Ochoa et al., 2025), while 32 were from our field samples collected in the CSMR (locations shown in Figure 1a) to better represent marsh soils in the spectral unmixing process. MESMA models the per-pixel fractional composition of each input endmember class using the quality of the spectral fit from the input endmember spectra to find the best fit model (Roberts et al., 1998; Ochoa et al., 2025). Our three-endmember MESMA implementation here unmixed both sets of AVIRIS surface reflectance imagery, employing a brightness normalization rather than shade endmember (Ochoa et al., 2025). This output estimates of brightness-normalized per-pixel fractional cover for each of the 206 endmember samples as well as total fractional cover for each of the three endmembers—GV, NPV, and soil. Because surface biofilms can contribute to green reflectance via photosynthetic algae presence similarly to vegetation, we treated high-GV fractional cover as a criterion for excluding pixels from the soil-dominant retrieval domain. The MESMA products provide continuous per-pixel fractional cover estimates

for NPV, GV, and soil (Figure 2); the soil fraction layer was used to identify soil-dominated pixels, and only pixels with soil fractional cover greater than 0.50 were retained for salinity retrieval and subsequent analyses. As salinity predictions were restricted to soil-dominated pixels, this reduced sensitivity to vegetation- or biofilm-dominated surfaces.

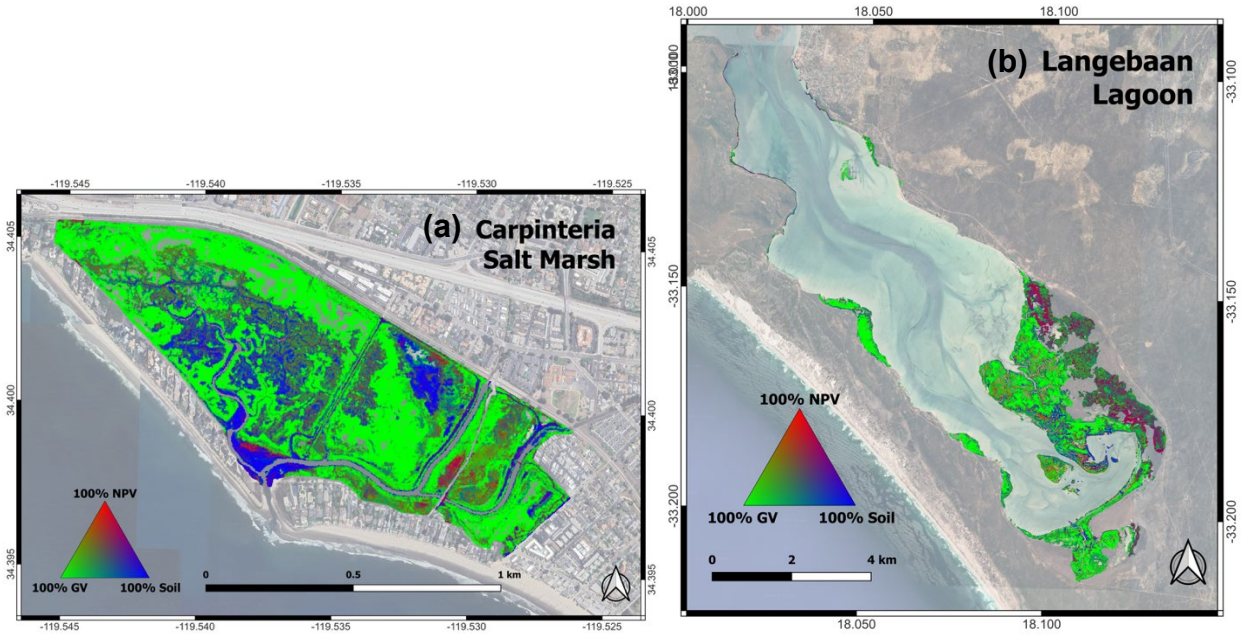


Figure 2: False color composite of Multiple Endmember Spectral Mixture Analysis (MESMA) fractional cover estimates for **(a)** the Carpinteria Salt Marsh Reserve and **(b)** the Langebaan Lagoon. The composite visualizes the three MESMA endmember fractions as RGB channels—red = non-photosynthetic vegetation (NPV), green = green vegetation (GV), and blue = soil—such that brighter blue tones indicate higher soil fractional cover. Per-pixel fractional cover values for each endmember are scaled from 0 to 1 (i.e., 0-100% cover). Submerged pixels were masked based on a Normalized Difference Water Index (NDWI; Equation 5).

We performed a threshold sensitivity analysis to refine the minimum MESMA-derived soil fraction used to classify pixels as soil-dominated prior to applying the PLSR salinity retrieval. Candidate minimum soil fraction thresholds (evaluated from 0.10–0.95) were tested in both the CSMR and Langebaan Lagoon data by sampling AVIRIS reflectance spectra from pixels meeting each threshold and computing nearest-library spectral angle (SA) to the *in situ* soil

389 spectral library used for model calibration. For each threshold, we summarized the median and
390 95th percentile SA values and quantified the corresponding change in spatial coverage. In the
391 Carpinteria analysis, Spectral Angle Mapper (SAM) metrics remained relatively stable at
392 moderate-to-high soil fractions but began to degrade at lower soil fractions (i.e., below ~0.50),
393 consistent with increasing mixed-pixel influence and reduced similarity to the soil training
394 spectra. In Langebaan, SAM values were comparably stable across low-to-moderate thresholds
395 through 0.50, while higher thresholds primarily reduced the number of eligible pixels without
396 yielding improved spectral similarity. This indicated that using 0.50 as a minimum soil cover
397 threshold across both sites retained sufficient spectral similarity to the *in situ* soil reflectances.
398 For both the fractional cover and soil salinity map products generated here, we applied a
399 water mask generated from the Normalized Difference Water Index (NDWI) at each site, as per
400 Equation 5:
401 $$NDWI = \frac{R_{green} - R_{SWIR}}{R_{green} + R_{SWIR}} \quad (5)$$
402 where R_{green} corresponds to the 560.51 (AVIRIS-3) and 562.52 nm (AVIRIS-NG) bands,
403 and R_{SWIR} corresponds to the 1611.39 (AVIRIS-3) and 1609.33 nm (AVIRIS-NG) bands. A
404 threshold applied to generate the masks, such that NDWI > 0.1 was designated as water (Figure
405 S1). Pixels classified as submerged using the NDWI threshold were masked from all subsequent
406 data products and analyses, including the MESMA fractional-cover composites (Figure 2). This
407 ensured that we only applied estimated soil salinity in non-submerged pixels.
408 To provide independent support for MESMA-derived soil fraction estimates, we
409 validated Carpinteria soil fraction outputs against plot-scale visual estimates of percent soil cover
410 collected along 4 transects (11 plots per transect, 5 m spacing). At each plot, the percent cover of
411 soil, GV, NPV, and water (if applicable) within a 0.25 m^2 quadrat was estimated visually. For the

soil cover validation, we excluded plots where either visual soil cover or AVIRIS-derived soil cover was <10%. The remaining dataset (n = 27) showed moderate agreement (R^2 = 0.47; MAE = 15.21%; Figure S2). Taken together, the Carpinteria validation and the threshold sensitivity analyses support using a single, physically interpretable soil-dominance cutoff across both sites. We therefore defined exposed (soil-dominated) pixels as those with MESMA soil fraction ≥ 0.50, finding that these pixels retain sufficient spectral similarity to pure soil reflectance measurements for the PLSR model to be applicable. We applied a Savitzky-Golay filter (Savitzky & Golay, 1964) to the reflectance imagery from both sites to smooth image noise while optimally retaining spectral shape and absorption features associated with given wavelengths. We then applied the PLSR model to the first derivative of reflectance within this domain to estimate surface soil salinity. Predicted values were converted from g salt g^{-1} dry soil to parts per thousand (ppt).

2.3.1. Additional Tests for Transferability of Soil Salinity Retrieval: Interpolation and Modeling with Unmixed Soil Reflectance Spectra

While our primary analysis and products are limited to pixels where soil cover is at least 50% to provide a reliable soil salinity retrieval, we explored the implementation of additional algorithmic steps to expand the valid spatial retrieval domain. First, we used bilinear interpolation to estimate soil salinity across both wetland domains and capture the landscape-scale distributions that are otherwise inhibited by vegetation cover. Spatial interpolation was used as a secondary analysis to infer salinity patterns between qualifying soil-dominated retrieval pixels and assess the uncertainty associated with extending the retrieval beyond its directly observed domain. Because the interpolated surfaces provide estimates at all field locations, their validation used the single interpolated pixel corresponding to each sampling location.

To evaluate whether the valid soil salinity retrieval domain could be extended into more highly mixed pixels, we additionally tested an approach that estimates the soil reflectance component using MESMA-derived fractional cover. This analysis assessed whether isolating the soil spectral signal from vegetation contributions could support salinity retrieval at lower soil fractional cover and thereby broaden the spatial applicability of the primary retrieval framework. To do so, we employed the MESMA fractional cover outputs (Figure 2) to estimate the soil reflectance component within each pixel by removing the modeled contributions of GV and NPV from the observed surface reflectance. This framework allowed us to test whether soil salinity could be estimated from unmixed soil spectra across a broader range of soil fractional cover and thereby assess the feasibility of reducing vegetation-driven bias.

For each pixel, MESMA provides brightness-normalized fractional cover estimates for soil, GV, and NPV. Assuming a linear mixing model, the observed reflectance spectrum R_{obs} can be expressed as:

$$R_{obs} = f_{soil}R_{soil} + f_{GV}R_{GV} + f_{NPV}R_{NPV} \quad (6)$$

where f_i represents the fractional cover of each component. Using the modeled endmember spectra and fractional cover estimates, we solved for the soil reflectance component R_{soil} by subtracting the vegetation contributions and dividing by the soil fraction:

$$R_{soil} = \frac{R_{obs} - f_{GV}R_{GV} - f_{NPV}R_{NPV}}{f_{soil}} \quad (7)$$

The resulting estimated soil reflectance spectra were then processed using the same spectral preprocessing workflow applied to the exposed-soil analysis to ensure methodological consistency. First, Savitzky–Golay filtering was applied to reduce high-frequency noise while preserving absorption features and spectral shape. Continuum removal was subsequently performed separately across the visible-near-infrared (VNIR), shortwave-infrared 1 (SWIR1),

and SWIR2 spectral regions to enhance diagnostic absorption features and reflectance characteristics potentially associated with salt mineral presence. The first derivative of the continuum-removed reflectance spectra was then calculated on the continuum-removed spectra, increasing sensitivity to spectral slope and absorption features.

The previously trained PLSR model was updated and trained using the first-derivative of the continuum-removed *in situ* soil reflectance spectra, convolved to the respective AVIRIS spectral response functions. The updated model was then applied to the unmixed soil reflectance spectra for each pixel. This approach allowed us to evaluate whether the model trained on pure soil spectra could generalize to soil reflectance estimated through spectral unmixing.

As with the exposed-soil workflow, predicted salinity values were converted from g salt/g dry soil to ppt for consistency with validation data. To evaluate the performance of this extended approach, we conducted validation using the same *in situ* soil salinity datasets employed in the primary analysis. We evaluated minimum soil fractional-cover thresholds from 0.10 to 0.95 in 0.05 increments and compared retrieval performance at each threshold using R^2 and mean absolute error (MAE). The final unmixed-soil retrievals were restricted to pixels with soil fractional cover ≥ 0.50, consistent with the threshold providing the strongest validation performance. Field-to-image validation then followed the same procedure used for the primary retrieval, averaging qualifying pixels within a three-pixel radius of each sampling location. At CSMR, we additionally evaluated the single qualifying coincident pixel at each field location. This analysis enabled comparison between (1) the original soil salinity retrieval and (2) the unmixed-soil retrieval while assessing whether spectral unmixing could reduce vegetation-related mixed-pixel effects and expand the valid retrieval domain.

2.4. Hydroperiod

While the airborne AVIRIS instruments provide ideal remote sensing data for investigating soil salinity distributions in coastal wetlands with their high spatial resolutions and number of spectral bands, orbital SAR allows us to investigate the hydrology driving those distributions. We thus used data from the Sentinel-1 satellite constellation to calculate hydroperiod—the percentage of time spent inundated per pixel—across the CSMR and Langebaan Lagoon.

2.4.1. Sentinel-1 SAR Data

To map flood frequency using SAR acquisitions, we used Sentinel-1 vertical transmit-vertical receive (VV)-polarized σ^0 backscatter time series, following Belhadj-aissa et al. (2026). Sentinel-1 operates in dual-polarization mode, transmitting in vertical polarization (V) and receiving in both vertical (VV) and horizontal (VH). For this study, and in general for water/land mapping with SAR, we use VV polarization due to its enhanced sensitivity to specular and double-bounce scattering mechanisms, which are particularly relevant for water surface detection (Henderson and Lewis, 2008). The dataset includes Sentinel-1 acquisitions for the year 2018, when Sentinel-1B was still operating alongside Sentinel-1A allowing a 6-day repeat pass. Level 1 Ground Range Detected (GRD) High-Resolution images- which include only the amplitude component of the complex signal- were downloaded as Radiometrically Terrain Corrected (RTC) products using the Hybrid Pluggable Processing Pipeline (HyP3) Python Software Development Kit (SDK) provided by the Alaska Satellite Facility.

RTC processing, performed using the GAMMA software, included terrain flattening based on the GLO-30 Copernicus digital surface model and speckle noise reduction via the Lee filter. The final RTC images were distributed as GeoTIFFs with a 10-meter pixel spacing. The area of interest was defined using the wetland domain boundaries for both the CSMR and

Langebaan Lagoon. This masking step excluded urban and built-up areas, minimizing high backscatter contributions from other targets and ensuring that the analysis concentrated on hydrologically relevant targets.

2.4.2. Preprocessing and SAR Flood Occurrence Mapping

In SAR imagery, open water surfaces typically exhibit low backscatter (appearing dark), while land surfaces show higher values due to volume or double-bounce scattering. Within the defined area of interest, which includes only wetlands and water bodies, the distribution of backscatter values is expected to be bimodal corresponding to water and dry land. Even in wetland environments, vegetated surfaces or tidal flats generally have a higher backscatter than open water. Still, under certain environmental conditions, such as wind-induced surface roughness, water bodies may exhibit increased backscatter, impairing the water/land discrimination. To mitigate such misclassification, we implemented a dynamic image filtering step where the backscatter histogram of each image is evaluated and only those scenes exhibiting a clear bimodal distribution—indicative of separable water and non-water classes—are retained.

Each retained image was then independently classified by identifying the local minimum between the two histogram peaks, producing a binary flood map distinguishing flooded (low σ^0) and non-flooded (high σ^0) pixels. These per-image classifications were subsequently aggregated to generate SAR-based flood frequency maps for both the CSMR and Langebaan Lagoon, representing the number of times each pixel was inundated over the observation period (Figure 6). With hydroperiod calculated for each study site we compared the soil salinity distributions to their respective inundation patterns to analyze the hydrologic drivers of salinity across these different hydroecological settings.

3. Results

3.1. Partial Least Squares Regression Model

The PLSR model, trained on the first derivatives of the *in situ* soil reflectance data convolved to AVIRIS-3's 7.4 nm spectral resolution, attained an R^2 of 0.90 and a mean absolute error (MAE) of 0.005 g salt/g dry soil. This PLSR model, based on the CSMR field data, was also re-trained to match AVIRIS-NG's 300 bands and 5 nm spectral resolution and attained an R^2 of 0.92 and an MAE of 0.004 g salt/g dry soil. Concurrently, we calculated the Variable Importance in the Projection (VIP) for each input band using the 7.4 nm PLSR model. High VIP values (here defined as VIP>1) denote higher model weighting and highlight important spectral features. With this threshold, here we identify important spectral features at ~416–453, 497–527, 654–706, 1138–1161, 1310–1340, 1979–2024, 2157–2202, and 2460–2497 nm (Figure 3).

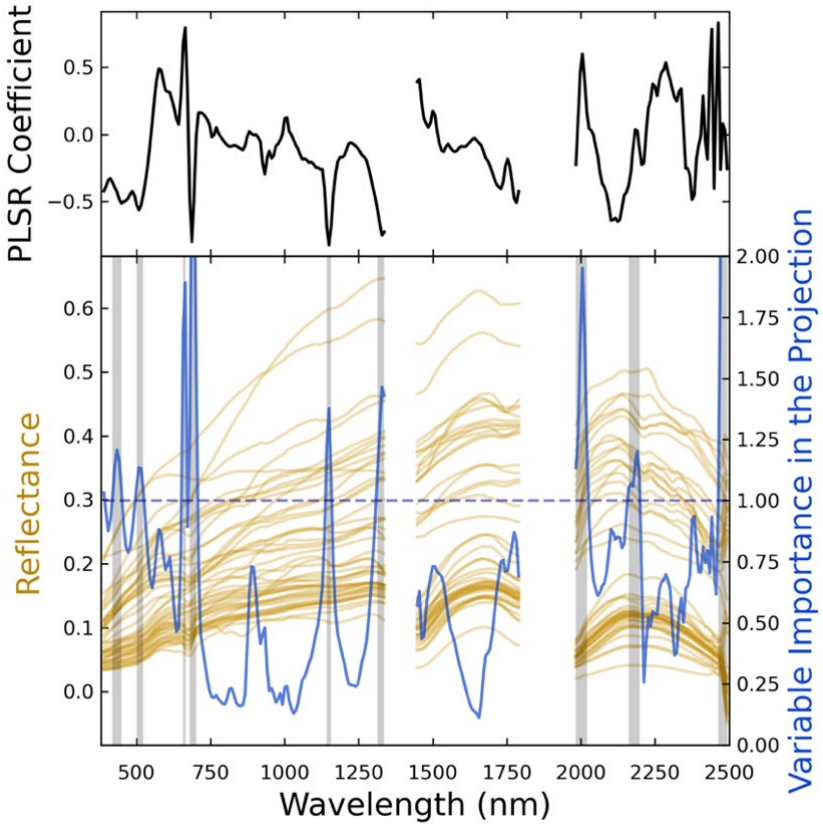


Figure 3: Partial Least Squares Regression coefficient values trained on *in situ* soil salinity for each band (top), and *in situ* reflectance samples with the Variable Importance in the Projection (VIP) values overlaid (bottom).

3.2. Soil Salinity Maps and Validation

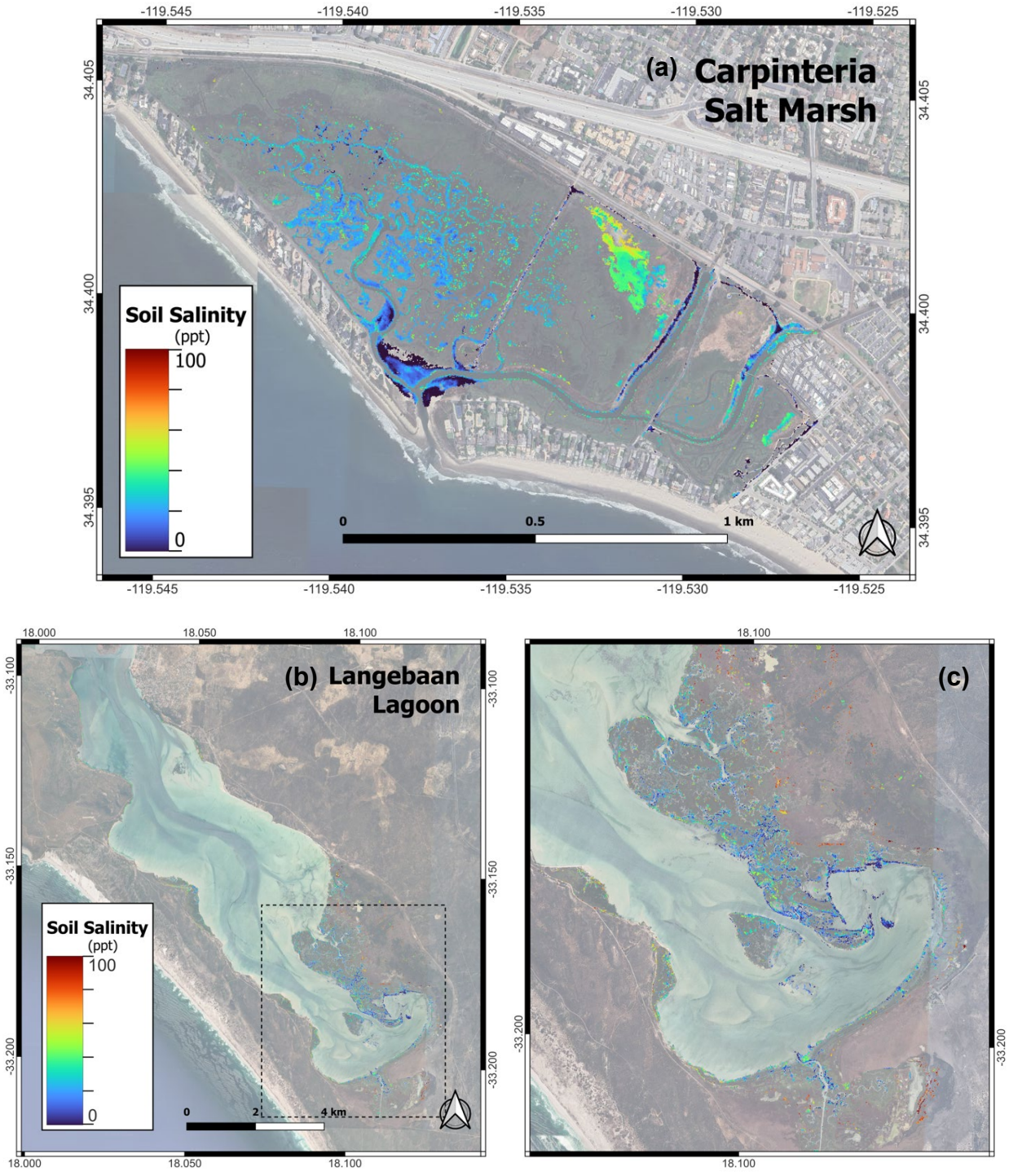


Figure 4: Soil salinity (parts per thousand) derived from **(a)** AVIRIS-3 across the Carpinteria Salt Marsh Reserve and **(b)** from AVIRIS-NG across the Langebaan Lagoon, with **(c)** an expanded view of the primary wetland area in the southern lagoon. Submerged pixels were

546 excluded using the Normalized Difference Water Index (NDWI) mask shown in Figure S1, and
547 retrievals are shown only for pixels with MESMA-derived soil fractional cover of at least 0.50.

548 With the methodology outlined above, we produced soil salinity maps (ppt) for both the
549 CSMR with AVIRIS-3 and Langebaan Lagoon in South Africa with AVIRIS-NG (Figure 4). We
550 validated the mapped salinity values for each site using available *in situ* salinity measurements.
551 The sampled sites in the Langebaan Lagoon study area were primarily located within vegetated
552 plots, resulting in an insufficient sample size for regression-based validation using only
553 qualifying coincident pixels at the sampling locations (MESMA-derived soil fractional cover
554 ≥0.50). For field-to-image validation, we instead identified qualifying retrieval pixels within a
555 three-pixel radius centered on each sampling location and averaged their salinity values. This
556 neighborhood averaging was applied only to the field-to-image comparison and did not alter the
557 native spatial resolution of the soil salinity products. At CSMR, validation using only the
558 qualifying coincident pixel at each sampling location yielded stronger performance ($n = 28$, $R^2 =$
559 0.79, MAE = 6.21 ppt) than the 7 × 7 neighborhood averaging, but excluded 4 of the 32 field
560 sites because the coincident pixels did not meet the ≥0.50 soil-cover criterion. The 7 × 7
561 neighborhood increased the number of qualifying CSMR validation sites to 32, yielding $R^2 =$
562 0.53 and MAE = 9.22 ppt (Figure 5a). At Langebaan Lagoon, 12 sites contained qualifying
563 salinity retrieval pixels within the 7 × 7 validation window. With all qualifying sites retained, the
564 AVIRIS-NG validation yielded $R^2 = 0.19$ and MAE = 18.64 ppt ($n = 12$). Because the Langebaan
565 validation included one high-residual observation that disproportionately influences summary
566 error statistics, we additionally report a sensitivity analysis excluding this point based on an
567 objective outlier criterion (values exceeding Q3 + 1.5 × IQR of the absolute residual distribution,
568 where Q3 is the 75th percentile value and IQR is the interquartile range). Excluding the single
569 IQR-identified high-residual observation improved performance to $R^2 = 0.67$ and MAE = 14.11

ppt (n = 11; Figure 5b). Accounting for this residual outlier, salinity map error metrics from the PLSR model and mapping method were thus similar across both the CSMR (the training/test site) and the Langebaan Lagoon (the independent test site).

As a secondary analysis, we evaluated full-extent bilinear interpolation of the original soil-dominated retrieval to estimate salinity across areas without qualifying retrieval pixels. At the CSMR, single-pixel validation of the interpolated AVIRIS-3 product yielded $R^2 = 0.67$ and MAE = 7.29 ppt (n = 32). At the Langebaan Lagoon, validation of the interpolated AVIRIS-NG product yielded $R^2 = -0.03$ and MAE = 16.08 ppt (n = 19); excluding the single IQR-flagged outlier improved performance to $R^2 = 0.54$ and MAE = 12.46 ppt (n = 18; Figures S3–S4).

Additionally, the model application using the MESMA-derived unmixed soil reflectance estimates produced lower performance metrics than the original soil-dominated reflectance approach, but still demonstrated some predictive capability. At the CSMR, the unmixed-soil retrieval yielded $R^2 = 0.27$ and MAE = 12.68 ppt using the 7 × 7 pixel neighborhood average (n = 32), and $R^2 = 0.13$ and MAE = 13.13 ppt using single coincident pixels (n = 28). At the Langebaan Lagoon, the 7 × 7 pixel validation yielded $R^2 = 0.22$ and MAE = 20.52 ppt (n = 12); excluding the single IQR-flagged outlier improved performance to $R^2 = 0.40$ and MAE = 18.00 ppt (n = 11; Figures S5–S6). These results indicate that the unmixed-soil approach retained some predictive capability but did not improve validation performance or extend the validated retrieval domain below the 0.50 soil fractional-cover threshold. Further analyses were therefore completed using the original soil-dominated model application.

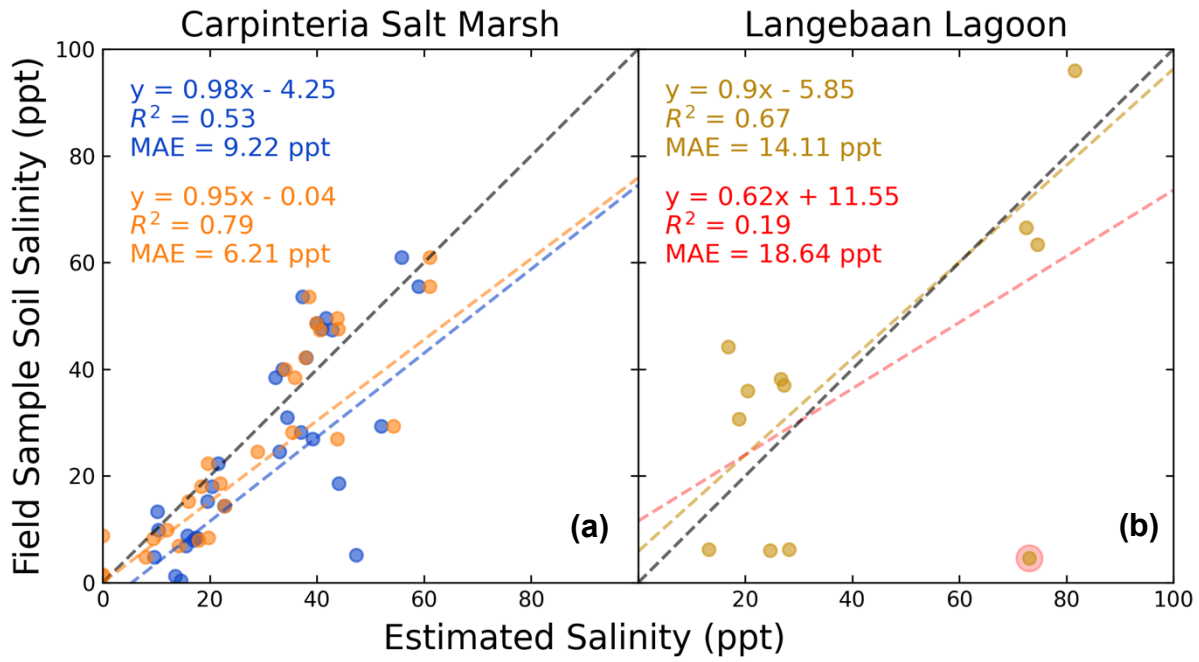


Figure 5: Validation of surface soil salinity estimates (ppt; maps shown in Figure 4) from the first-derivative reflectance PLSR model using **(a)** AVIRIS-3 at the Carpinteria Salt Marsh Reserve and **(b)** AVIRIS-NG at the Langebaan Lagoon. The dashed gray line denotes the 1:1 relationship, and dashed colored lines indicate least-squares fits. For the CSMR, we report the validation using both the 7 × 7 pixel neighborhood average (blue) and the single coincident pixel values. For Langebaan, we additionally report a sensitivity analysis excluding a single high-residual observation identified by an objective residual-based outlier criterion (Q3 + 1.5 × IQR of the absolute residuals; circled in red); regression statistics are shown both with (red) and without (orange) this point.

Table 2: Comparative model performances for predicting soil salinity

Model Application	n (Outlier-Removed n)	Validation Pixel Area	Parameters	R^2(Outlier-Removed R^2)	MAE(Outlier-Removed MAE; ppt)
PLSR (*In Situ* Calibration)*	32	-	First Derivative of Reflectance	0.90	5.00
AVIRIS-3 (Carpinteria, CA)*	32	7 × 7 Pixel Average	First Derivative of Reflectance, Soil Cover ≥ 50%	0.53	9.22

AVIRIS-3 (Carpinteria, CA)*	28	Single Pixel	First Derivative of Reflectance, Soil Cover ≥ 50%	0.79	6.21
AVIRIS-NG (Langebaan, ZA)*	12 (11)	7 × 7 Pixel Average	First Derivative of Reflectance, Soil Cover ≥ 50%	0.19 (0.67)	18.64 (14.11)
AVIRIS-3 (Carpinteria, CA)	32	Single Pixel	First Derivative of Reflectance, Full Extent Interpolated	0.67	7.29
AVIRIS-NG (Langebaan, ZA)	19 (18)	Single Pixel	First Derivative of Reflectance, Full Extent Interpolated	-0.03 (0.54)	16.08 (12.46)
PLSR (*In Situ* Calibration)	32	-	Continuum Removal, First Derivative of Reflectance	0.85	5.77
AVIRIS-3 (Carpinteria, CA)	32	7 × 7 Pixel Average	Unmixed Soil Reflectance, Continuum Removal, First Derivative of Reflectance, Soil Cover ≥ 50%	0.27	12.68
AVIRIS-3 (Carpinteria, CA)	28	Single Pixel	Unmixed Soil Reflectance, Continuum Removal, First Derivative of Reflectance, Soil Cover ≥ 50%	0.13	13.13
AVIRIS-NG (Langebaan, ZA)	12 (11)	7 × 7 Pixel Average	Unmixed Soil Reflectance, Continuum Removal, First Derivative of Reflectance, Soil Cover ≥ 50%	0.22 (0.40)	20.52 (18.00)

*Selected PLSR model and validated model applications

3.3. Relationships Between Soil Salinity and Hydroperiod

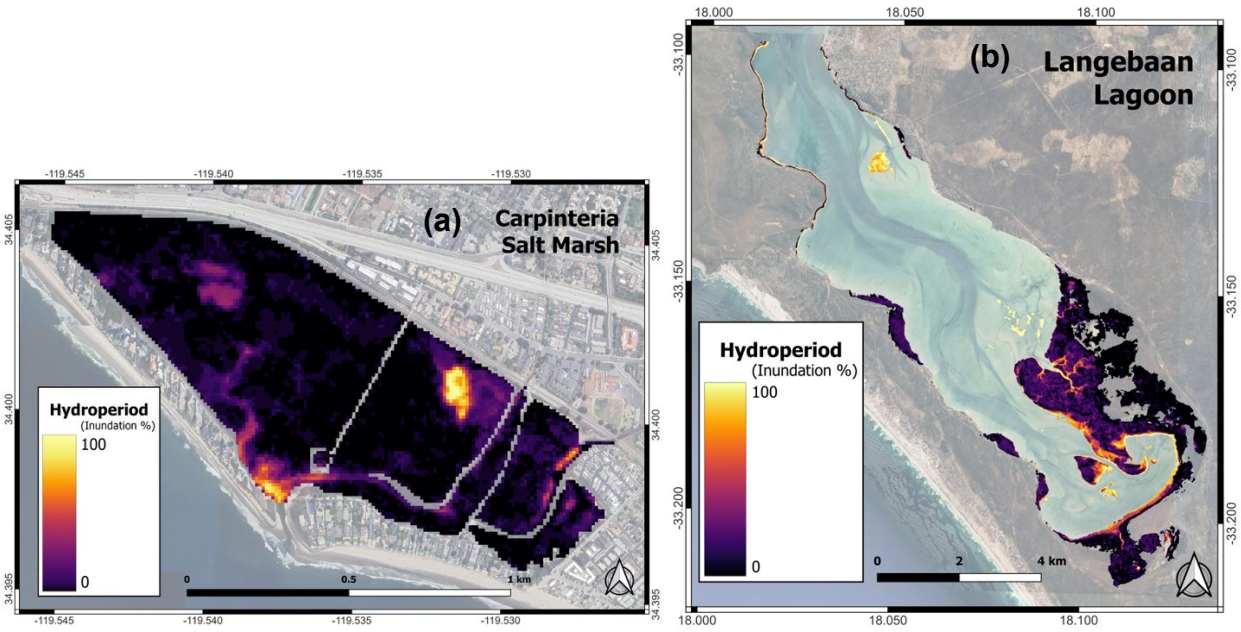


Figure 6: Hydroperiod (% time spent inundated) derived from Sentinel-1 across **(a)** the Carpinteria Salt Marsh Reserve and **(b)** the Langebaan Lagoon.

Each hydroperiod map shows the percentage of the Sentinel-1 timeseries that each wetland pixel spent inundated (Figure 6), a key parameter for understanding each site's hydrologic regime and its corresponding ecological relationships to salinity. To understand how hydroperiod drives salinity distributions at each site, we compared each hydroperiod map to the corresponding salinity map after resampling to the Sentinel-1 products' 10 m spatial resolution. Here we assessed the soil salinity maps containing only pixels where soil cover ≥ 50%, thereby excluding lower soil cover pixels in the comparison with hydroperiod. We divided the hydroperiod values into 15 bins of 4% each, calculating the mean and standard deviation for the soil salinity values in each bin. We then fit quadratic functions to the binned mean soil salinity values, such that hydroperiod is the independent variable and soil salinity is the dependent variable. The fitted quadratic functions are shown in Figure 7 with the CSMR showing a significant positive quadratic relationship between hydroperiod and soil salinity ($R^2 = 0.84$, MAE = 2.40 ppt, $p < 0.001$). Conversely, South Africa's Langebaan Lagoon shows a significant

negative relationship (R^2 = 0.92, MAE = 2.36 ppt, $p < 0.001$). Figure 7 also overlays *in situ* salinity measurements with the remotely derived hydroperiod value extracted at each sampling location, alongside the binned AVIRIS salinity retrievals. The field dataset is limited in sample number and spatial coverage relative to the full hydroperiod gradient—a key difficulty for field-based landscape-scale analysis—and is therefore insufficient to resolve hydroperiod-driven patterns. The *in situ* point measurements show no clear relationship with hydroperiod, whereas the binned remote-sensing product values show consistent hydroperiod–salinity trends across both sites.

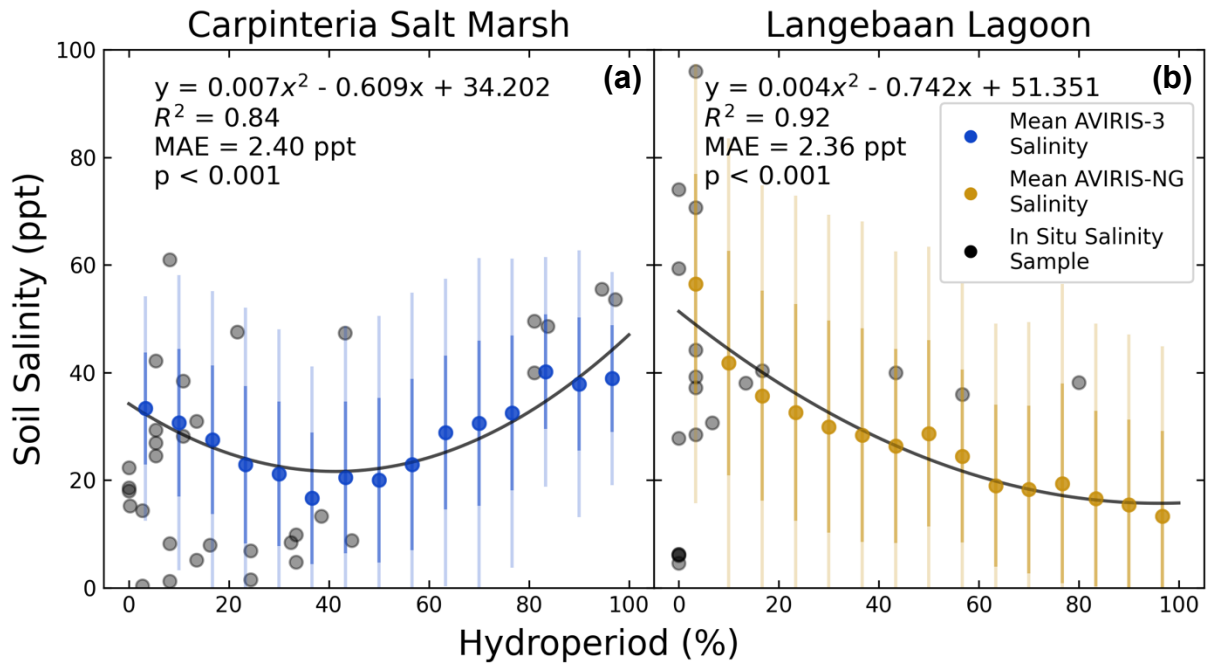


Figure 7: Hydroperiod (% time spent inundated) derived from Sentinel-1 across **(a)** the Carpinteria Salt Marsh Reserve and **(b)** the Langebaan Lagoon. Each colored point represents the mean salinity value for the given bin, with the bars representing 1 and 2 standard deviations around the mean value for each bin. The field sample soil salinity values and their corresponding hydroperiod pixel values are shown overlaid in black.

4. Discussion

4.1. Model Performance, Error Sources, and Limitations

This study demonstrates the capability of airborne imaging spectroscopy for mapping soil salinity in dynamic coastal ecosystems. Our PLSR model (trained on *in situ* soil salinity sample and reflectance data from the CSMR) and mapping methodology produced comparable results (Figure 5) when applied to imaging spectrometer data collected over both the training site (CSMR: n = 32, R^2 = 0.53, MAE = 9.22 ppt) and the independent test site (Langebaan Lagoon; n = 12, R^2 = 0.19, MAE = 18.64 ppt, improving to n = 11, R^2 = 0.67, and MAE = 14.11 ppt when the single IQR-identified high-residual observation was excluded). We thus demonstrate this model's transferability from one coastal wetland to another, which may offer future opportunities in using a generalized soil salinity retrieval algorithm capable of monitoring estuarine salinity dynamics.

Across both sites, applying the PLSR model to MESMA-derived unmixed soil reflectance produced validation performance generally weaker than the original soil-dominated reflectance approach, though it retained some predictive capability, with both methods performing best when restricted to applicable soil pixels (soil fractional cover ≥0.50; Table 2). The analysis demonstrated that soil-signal isolation is feasible, but did not improve validation performance or extend the validated retrieval domain below 0.50 in its present implementation. Although the unmixed-soil salinity maps exhibited greater spatial variability and apparent noise than the original products, the retained predictive capability suggests that soil-signal isolation via spectral unmixing is a promising pathway for extending retrieval into more mixed pixels and warrants further refinement in future work.

While we validated results from two study sites, several uncertainties and limitations remain. The primary salinity maps and associated hydroperiod and vegetation analyses were restricted to non-submerged pixels with soil fractional cover ≥0.50 and therefore did not rely on

interpolation. Bilinear interpolation was retained only as a secondary analysis to explore the potential for extending retrieval-derived salinity patterns into more vegetated portions of the wetlands. These interpolated values are less certain because they are inferred from surrounding soil-dominated pixels and may not capture local controls such as vegetation, microtopography, hydrologic connectivity, and flushing. Uncertainty is therefore expected to increase in areas farther from qualifying retrieval pixels or with dense and spatially heterogeneous vegetation, and the interpolated products should not be interpreted as directly validated salinity retrievals. The interpolation may also miss variations in microtopography and vegetation that influence wetland hydrology and soil salinity, including plant-driven differences in evapotranspiration, sediment trapping, and root-zone water and ion dynamics that are not represented by retrievals from soil-dominated pixels.

This study is also limited by the relatively small sample size of training and validation data. Additional sampling of soil salinity across coastal habitat types that accounts for vegetation cover, elevation, and hydrology is recommended to improve on our dataset and algorithm to build towards a fully generalized soil salinity retrieval algorithm. Such additional datasets and analyses will likely improve further on our exploration of estimating unmixed soil reflectance, which showed weaker validation performance than our original model while retaining some predictive capability, as a basis for model development and application. However, our results with this unmixed approach did not show an improvement to the applicable minimum soil cover threshold (0.50), while also increasing the noise level in the mapped salinity retrievals. While the independent validation results from the Langebaan Lagoon show lesser performance than the CSMR soil salinity map, the fact that errors remained of a similar magnitude to results from a dataset not trained with any local data shows the promise of a generalized model and that these

682 impacts may be addressed with additional data. Existing error is likely influenced by the
683 difference between *in situ* sampling dates and imagery collection. It should also be noted that the
684 linear fit and corresponding error metrics in the Langebaan Lagoon are disproportionately
685 influenced by a single high-residual observation (sample value 4.65 ppt). This point lies on a
686 transition zone along the upland area of the Lagoon's southern wetlands, where there appear to
687 be steep salinity gradients due to microtopography and in turn enhancing the error potential.
688 Sensitivity analysis that accounted for this point's residual being a significant outlier showed a
689 robust soil salinity retrieval with the remaining datapoints (Table 2). Despite this singular point,
690 our overall validation indicates that our model is robust and properly trained on the spectral
691 signature of salts deposited within the top layer of soil. Overall, this analysis and the independent
692 validation support the feasibility of a transferable algorithm for modeling and mapping soil
693 salinity in coastal ecosystems, while also highlighting the need for additional training and
694 validation data and improved soil-signal isolation to extend the approach across more densely
695 vegetated wetland areas.

696 Recent studies demonstrate that incorporating environmental proxies can substantially
697 improve site-specific salinity prediction. Silva et al. (2025) combined AVIRIS-NG imaging
698 spectroscopy with Light Detection and Ranging (LiDAR)-derived elevation and vegetation
699 spectral indices in a random forest framework to estimate root-zone soil salinity, reporting R^2 =
700 0.86 using elevation alone and R^2 = 0.73 when combining elevation with spectral indices. Their
701 results highlight the strong topographic control on salinity gradients within that marsh system.
702 Similarly, Sui et al. (2022) integrated vegetation indices, terrain attributes, hydrological
703 connectivity metrics, and temporal variables within a random forest model to predict surface soil
704 salinity in the Yellow River Delta, achieving R^2 = 0.89 (RMSE = 1.48 g kg^{-1}) under 10-fold

cross-validation. These approaches demonstrate that incorporating elevation, vegetation condition, and hydrological context can enhance predictive accuracy where salinity is tightly coupled to site-specific environmental gradients. However, reliance on vegetation indices, hydrological connectivity metrics, and locally calibrated elevation–salinity relationships introduces potential limitations for transferability across sites with differing hydrogeomorphic settings, plant communities, or management histories. In contrast, our framework is based on the reflectance characteristics of the soil surface itself, targeting spectral features associated with salt presence rather than proxy variables. While this may yield more moderate predictive performance in some contexts, it reduces dependence on site-specific environmental covariates and thus represents a step toward a more generalized and transferable imaging spectroscopy–based soil salinity retrieval algorithm.

4.2. Spectral Signatures and Variable Importance

While NaCl is commonly a dominant contributor to salinity in tidally influenced coastal wetland soil due to seawater inputs and tidal inundation, other major ions and salts (including Mg^{2+} and SO_4^{2-} species) can contribute substantially to overall salinity level and have important ecological impacts. Differences in ionic composition can also alter mineral solubility and chemical equilibria in wetland soils, affecting the availability and cycling of nutrients and trace elements beyond the effects of total salinity alone (Herbert et al., 2015). Though coastal wetland plant species are adapted with different salt tolerances, elevated salinity can cause osmotic stress in plants and reduce water uptake, as well as altering microbial activity and nutrient cycling (Rath and Rousk, 2015). In addition, sulfate reduction under anoxic conditions can generate hydrogen sulfide (H_2S), a potent phytotoxin that can inhibit root metabolism and restructure microbial communities in wetland soils (Lamers et al., 2013).

The PLSR model, based on first derivatives of the in situ reflectance spectra, was tuned to wavelength regions consistent with spectral structure associated with salt-affected soils and hydration-sensitive surface conditions. This is evident in the VIP scores (Figure 3), where bands with VIP > 1 occur in regions consistent with hydration-related SWIR structure reported for chloride and sulfate salts and salt–soil mixtures. Cerubini et al. (2022) show that anhydrous NaCl is largely featureless in the VNIR, whereas hydrated chloride and sulfate salts and saline surfaces can exhibit stronger SWIR absorption structure associated with bound/structural water. In our model, VIP>1 clusters occur at ~1.98–2.02 μm and ~2.16–2.20 μm (with additional weighting near ~2.46–2.49 μm), consistent with sensitivity to hydration-state structure and soil–salt mixture effects in the SWIR. Portions of the ~1.9–2.0 μm region may also covary with sample moisture and associated hydration-state effects, influencing spectral slope and derivative structure in shoulder regions adjacent to strong water absorptions. Elevated VIP in visible wavelengths may reflect co-varying surface biological material (e.g., cyanobacterial/algal films; Karnieli et al., 1999) and/or soil brightness and color effects, which may limit transferability across sites. Accordingly, our retrieval is constrained to soil-dominated pixels and we emphasize SWIR structure associated with salts and hydration rather than visible-band signals alone, though visible-band weighting may also help the model remain robust to variability in surface biofilms present within the calibration data.

Soil texture, mineralogy, and organic matter can also influence reflectance magnitude and spectral slope and may therefore contribute to unexplained variance in the salinity–reflectance relationship, as salts typically comprise a relatively small fraction of total soil mass. Soil physical properties that influence moisture retention and hydraulic connectivity (e.g., texture-driven differences in drainage and conductivity) can modulate salinity patterns along elevation and

hydroperiod gradients (Moffett et al., 2010; Wang et al., 2007). Although we did not quantify grain size distributions or mineralogical composition for individual samples, our field sampling was designed to span the range of visually apparent exposed-soil substrate types and surface conditions present during the overflight—including finer-textured and sandier-appearing surfaces, variability in organic material and surface biofilms, and a range of wetness states (Table 1)—to reduce bias toward a single soil background. In combination with the derivative-based preprocessing and the PLSR modeling, this broad sampling strategy helps ensure that the model is tuned primarily to spectral structure that covaries with salt presence rather than to site-specific brightness or texture effects alone (Cerubini et al., 2022; Karnieli et al., 1999). Although anhydrous NaCl lacks strong diagnostic absorptions across much of the VSWIR, salt accumulation can still alter soil spectra through broad increases in albedo, salt–soil mixture effects, and changes in continuum slope. The VIP pattern therefore suggests that the PLSR model exploits salt-affected spectral structure while also weighting wavelengths that may account for co-varying surface conditions (e.g., moisture/hydration state, surface biofilms in the visible, and soil matrix/mineral variability near ~2.2 μm), thereby improving robustness across heterogeneous marsh surfaces. Future work pairing soil reflectance measurements with both salinity and explicit soil property measurements would further strengthen generalization across substrate classes and geographic settings.

4.3. Soil Salinity and Hydroperiod Distributions

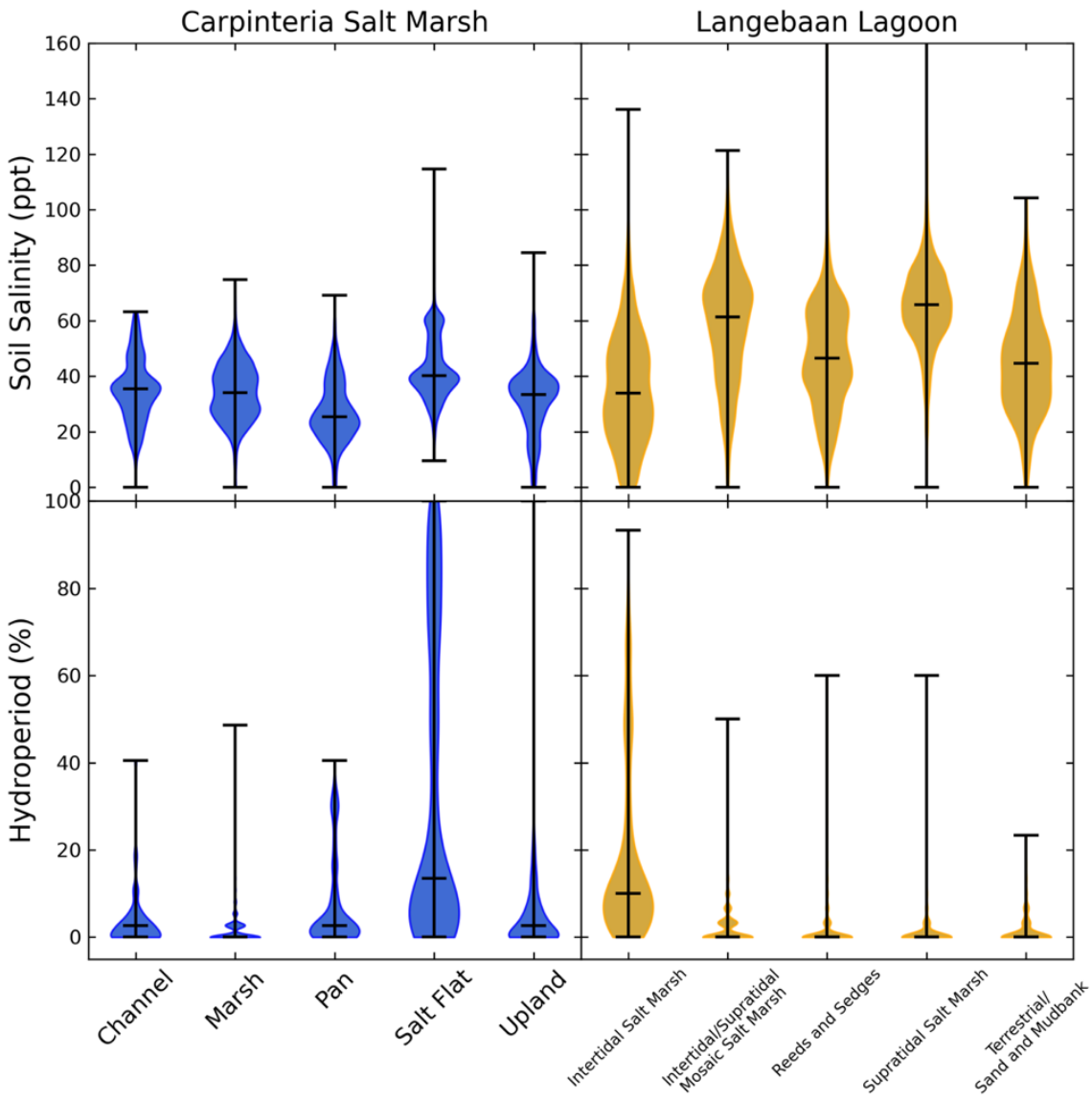


Figure 8: Violin plots showing soil salinity and hydroperiod distributions across the different habitat types in the Carpinteria Salt Marsh Reserve and Langebaan Lagoon.

Our map products in conjunction with habitat type data reveal the distributions of soil salinity and hydroperiod within each class for both the CSMR and the Langebaan Lagoon (Figure 8). We used shapefiles containing polygons for various habitat types to generate random points (2500 per habitat type for the CSMR, 5000 for Langebaan) in each study area. We extracted the corresponding salinity and hydroperiod values for each point, compiling a robust set of values within each habitat polygon for each data product. For the CSMR, we used a

779 shapefile containing five habitat types—channels, pans, marsh, salt flats, and upland—where
780 pans are low-lying, intermittently ponded depressions within the marsh, and salt flats are higher-
781 elevation, sparsely vegetated to unvegetated surfaces characterized by persistent salt crusts and
782 high surface salinity (Lafferty et al., 2017). For the Langebaan Lagoon we used a shapefile (from
783 Van der Linden, 2014; data updated 2023) depicting similar habitats with more detailed wetland
784 vegetation types, including: Intertidal Salt Marsh, Intertidal/Supratidal Mosaic Salt Marsh, Reeds
785 and Sedges, Supratidal Salt Marsh, Terrestrial, and Sand and Mudbank (Van der Linden, 2014;
786 Adams et al., 2016; Adams et al., 2019). Specific species with dominant coverage for Intertidal
787 Salt Marsh (*Spartina maritima*) and Supratidal Salt Marsh (*Juncus kraussii*) from this habitat
788 map were grouped with their parent class. These habitat types, coupled with the salinity and
789 hydroperiod products, demonstrate the potential of our methodology to examine the ranges and
790 tolerances of different plant communities with respect to these ecological variables. This further
791 demonstrates the use of species' inherent salinity tolerance ranges to validate observed soil
792 salinity in the context of longer time scales.
793 The CSMR's salinity distributions appear to be driven by the influence of freshwater via
794 its channels in addition to saline tidal inundation. The CSMR is characterized by a series of
795 natural and artificial channels at the base of the Franklin and Santa Monica creeks. These streams
796 rarely have natural perennial surface flows across the coastal plain. Impermeable beds over
797 which groundwater sourced from rain, irrigation, and stream water flows occur near the surface
798 of the Carpinteria Salt Marsh. This causes discharge from the shallow groundwater into the
799 marsh's lower stream channels (Carpinteria Salt Marsh Reserve Management Plan). With salt
800 flats exhibiting both high estimated soil salinity and hydroperiod, it is likely that parts of the
801 marsh that are inundated in high tides are not exposed to this fresh groundwater flow and are not

802 well drained, causing the saline water to pool for extended periods of time and deposit salts on
803 the surface. This explains the CSMR's positive quadratic relationship between soil hydroperiod
804 and soil salinity (Figure 7) and the high salinity and hydroperiod distribution values in the violin
805 plot relative to the other classes (Figure 8).
806 Surface soil salinity distributions in the Langebaan Lagoon, conversely, decline with
807 hydroperiod. Wave-cut terraces overlain by aeolian dunes dominate the topography of the
808 Langebaan area, with sand-covered plains, fixed dunes, and surface limestone ridges forming the
809 visible landscape. Little freshwater surface runoff water enters Langebaan Lagoon. Freshwater
810 inputs are derived through discharge from the Elandsfontein Aquifer System, which is comprised
811 of a lower unit that lies on a basement rock formation and an upper unit located in consolidated
812 sands and calcretes separated by an impermeable layer of clay (DWAF, 2008). However, the clay
813 layer thins out towards the Langebaan Lagoon and groundwater from the upper and lower
814 aquifers is discharged there. Isotope analysis confirmed that a hydraulic connection exists
815 between the Elandsfontein aquifer and the lagoon (Israel et al., 2021), forcing groundwater to
816 flow towards the surface at the lagoon edge and resulting in significant groundwater outflow to
817 the lagoon (DWAF, 2008). The possibility that the interaction between the Elandsfontein aquifer
818 and the lagoon exists is corroborated by fluctuating water levels and changes in water quality
819 linked to tidal movements (Israel et al., 2021). Inundation patterns, as captured in the
820 hydroperiod, are largely driven by tidal variability (Figure 6), while groundwater acts as a
821 'dilution factor' at key locations, moderating the impact of evaporation in this arid environment
822 on soil salinities. Given that tidal inundation is the main driver of Langebaan Lagoon's
823 hydroperiod ranges, the negative relationship was to be expected with soil salinity increasing
824 with reduced tidal inundation, with intertidal soil salinity values generally similar or slightly

above that of seawater. Groundwater or rainfall can result in localized soil salinity values lower than that of seawater, but given the arid nature of the coast most intertidal measurements are dominated by marine inputs. Diluting effects are generally observed sub-surface levels of 0.5 – 1.5 m depth. This is apparent in the intertidal zone of the Langebaan Lagoon's largest continuous marsh area on its northeast shore, where soil salinity values range from approximately 10-30 ppt. This is lower than previous measurements in the intertidal zone (Van der Linden, 2014) and is likely driven by a wet spring 2023 season and an October storm. In fact, measurements of groundwater depth across two boreholes in the Geelbek area of the southern Langebaan Lagoon show increasing groundwater levels from October 11 to 24, 2023. These boreholes show water levels increasing from 1.31 to 1.28 and 0.74 to 0.70 meters below ground level (mbgl) across these dates, respectively. A third nearby borehole, however, shows the groundwater level decreasing slightly from 0.75 to 0.77 mbgl. As these data show a general increase in groundwater levels, it is likely that additional regional runoff likely led to higher-than-average fresh groundwater flowing through the wetland system, flushing and diluting the intertidal zone as it flowed into the lagoon. Recent assessments of South Africa's wetlands identify hydrologic alteration as a primary driver of degradation and emphasize the need for improved monitoring to quantify resulting water-quality impacts (Van Niekerk et al., 2022; Van Deventer et al., 2025). The hydroperiod–salinity patterns we observe at Langebaan Lagoon underscore the value of landscape-scale mapping to detect hydrologic alteration and resulting changes in salinity patterns in managed wetland systems.

Our observed salinity–hydroperiod relationships are consistent with established conceptual and modeling work showing that marsh salinity patterns emerge from the coupled effects of inundation frequency, drainage, evaporation, and topographic position. Salt marsh

zonation has been shown to track spatial gradients in soil moisture and salinity that covary with elevation and hydroperiod, with vegetation patterns reflecting these underlying physical controls (Moffett et al., 2010). Process-based modeling likewise predicts strong salinity structure along topographic gradients—where frequent tidal inundation promotes flushing and limits salt accumulation, whereas less frequently flooded or poorly connected areas experience reduced flushing and greater evapoconcentration—thereby producing localized salinity maxima and persistent spatial contrasts (Wang et al., 2007). These mechanisms also provide context for the formation and persistence of salt barrens and salt pans, where elevated salinity can maintain unvegetated areas and inhibit plant encroachment (Qi et al., 2017), and for broader syntheses linking climatic forcing and evaporative demand to marsh salinity stress and landscape patterning (Pennings & Bertness, 1999). In this context, the positive quadratic relationship between hydroperiod and soil salinity observed at the CSMR is consistent with a regime in which longer inundation duration and reduced drainage coincide with enhanced salt retention and evaporative concentration in low-relief areas. By contrast, the relationship observed at Langebaan Lagoon whereby salinity decreases with hydroperiod suggests a system where more frequently inundated or hydrologically connected areas experience greater tidal exchange and flushing, limiting salt accumulation relative to less frequently flooded, more isolated surfaces.

As we demonstrate in these two study sites, our imaging spectroscopy-derived soil salinity retrieval method can be used to map soil salinity, enabling further analysis for coastal wetland monitoring and trend assessment. Our comparisons (Figures 7 & 8) highlight the value of imaging spectroscopy for revealing landscape-scale hydroperiod–salinity relationships and associated dynamics that are difficult to detect or quantify using point-based field measurements alone.

5. Conclusion

This study evaluated the potential for a generalized imaging spectroscopy–based approach to retrieve surface soil salinity in coastal wetlands and move towards automated monitoring over time, with our primary objective being to test whether salinity can be detected from exposed or soil-dominated pixels with sufficient accuracy and whether retrieval performance is transferable across sites. Across both study sites, our results support the feasibility of estimating surface soil salinity from soil reflectance characteristics and using these retrievals to characterize broader landscape-scale patterns. The directly validated retrieval domain was restricted to non-submerged pixels with MESMA-derived soil fractional cover ≥0.50, and the strongest support for the current method therefore applies to soil-dominated portions of coastal wetlands. We further tested our approach by estimating soil reflectance in mixed pixels using MESMA-derived fractions to remove vegetation components from the observed spectra, demonstrating the feasibility of soil-signal isolation as a pathway for mitigating vegetation impacts, although it did not improve retrieval performance in its present implementation. Together, these findings indicate that soil reflectance–based retrieval provides a physically interpretable foundation for salinity estimation and that continued refinement of soil-isolation strategies is a viable pathway toward a more generalized, transferable algorithm for coastal wetland monitoring.

In situ salinity sampling and wetland habitat mapping are costly and time consuming, often confining these efforts to small areas and infrequent surveys. The approach described here is well suited to scaling with current airborne imaging spectrometers (e.g., AVIRIS-class instruments) and to emerging spaceborne imaging spectroscopy missions that can provide repeat, regional-to-global coverage (e.g., EMIT, EnMAP, PRISMA, and forthcoming global missions

such as NASA's Surface Biology and Geology). These observations could add an important dimension to established monitoring tools by enabling earlier detection of salinity shifts linked to hydroperiod change. In the Langebaan Lagoon, where freshwater inputs are strongly influenced by groundwater discharge and regional groundwater extraction pressures, such capability could improve detection of hydrologic alteration within the Ramsar site wetlands. Key next steps include improving soil signal isolation in mixed pixels, quantifying and propagating uncertainty through retrieval and interpolation where necessary and evaluating performance across a wider range of wetland geomorphic settings, moisture conditions, and vegetation communities. These advances employing imaging spectroscopy to build on our approach and results would support assessment of climate and management-driven stressors—including sea-level rise, storm impacts, drought, and altered groundwater patterns—on coastal wetland resilience.

Acknowledgments

This work was funded by the *BioREaCH: Biodiversity-Remote sensing for Estuarine and Coastal Habitat* project (grant number NASA ROSES NNH21ZDA001N-BIODIV) as part of NASA's BioSCape campaign. We would like to acknowledge the University of California Natural Reserve System, UCSB Carpinteria Salt Marsh Reserve, for enabling us to collect data and utilize data from the Reserve. A portion of this research was carried out at the Jet Propulsion Laboratory, California Institute of Technology, under a contract with the National Aeronautics and Space Administration (80NM0018D0004). © 2026. All rights reserved.

Conflict of Interest Statement

The authors have no conflicts of interest to disclose.

Inclusion in Global Research

This study was conducted in South Africa as part of the BioSCape field campaign, a collaboration between South African and U.S. researchers and institutions supported by NASA, the National Research Foundation of South Africa (NRF), the South African Environmental Observation Network (SAEON), and UNESCO. The Langebaan Lagoon component of this work was carried out in collaboration with researchers at CSIR, the University of the Witwatersrand, Nelson Mandela University, and South African National Parks (SANParks). Field sampling in Langebaan Lagoon was conducted by ADC, AB, DJ, EA, LN, and PT. Additional GIS layers, in situ datasets, and site documentation were provided by HvD, LvN, JA, and RMF and were integral to the analysis and interpretation of the South African study site. Fieldwork was conducted within SANParks-administered lands under permit CRC/2023-2024/001, with prior notification to park staff and in accordance with their guidance. South African collaborators contributed significant site knowledge, data resources, logistical support, and scientific input throughout the study, and these contributions are reflected through co-authorship and institutional partnership.

Open Research

All remote sensing datasets used in this study are archived with the Oak Ridge National Laboratory Distributed Active Archive Center (ORNL DAAC and available to the public for download following registration via NASA EarthData (https://www.earthdata.nasa.gov/data/projects/bioscape/). The AVIRIS-3 data used for this study is available through Brodrick et al. (2025; https://doi.org/10.3334/ORNLDAAC/2357), and the AVIRIS-NG data is available through Brodrick et al. (2026; https://doi.org/10.3334/ORNLDAAC/2419). The wetland vegetation plot data containing the salinity measurements from the Langebaan Lagoon study site are available through Campbell et

al. (2025; https://doi.org/10.3334/ORNLDAAC/2441).The primary soil salinity raster products, hydroperiod raster products, and paired in situ soil sample and reflectance data from the Carpinteria Salt Marsh Reserve are available through Jensen et al. (2026; https://doi.org/10.3334/ORNLDAAC/2529).

References

Adams JB, Veldkornet D, Tabot P (2016) Distribution of macrophyte species and habitats in South African estuaries. S Afr J Bot 107, 5–11. https://www.sciencedirect.com/science/article/pii/S0254629916337887?via%3Dihub; Data DOI: https://doi.org/10.1016/j.sajb.2016.08.001.

Adams JB, Fernandes M., Riddin T (2019) Chapter 5: Estuarine Habitat Extent and Trend. In: Van Niekerk L, Adams JB, Lam-berth SJ, MacKay F, Taljaard S, Turpie JK, Weerts S, Raimondo DC (eds.) South African National Biodiversity Assessment 2018: Technical Report. Volume 3: Estuarine Realm. Council for Scientific & Industrial Research (CSIR) report number CSIR/SPLA/EM/EXP/2019/0062/A. South African National Biodiversity Institute (SANBI), Pretoria, South Africa. Pp. 52–75. Report Number: SANBI/NAT/NBA2018/2019/Vol3/A.

Adams JB. 2020. Salt marsh at the tip of Africa: Patterns, processes and changes in response to climate change. Estuarine, Coastal & Shelf Science 237: 106650. DOI: 10.1016/j.ecss.2020.106650.

Adams, K.H., Reager, J.T., Buzzanga, B.A., David, C.H., Sawyer, A.H. and Hamlington, B.D., (2024). Climate-induced saltwater intrusion in 2100: Recharge-driven severity, sea level-driven prevalence. Geophysical Research Letters, 51(22), p.e2024GL110359.

Adhikari, S., Ivins, E. R., Frederikse, T., Landerer, F. W., & Caron, L. (2019). Sea-level fingerprints emergent from GRACE mission data. Earth System Science Data, 11(2), 629–646. https://doi.org/10.5194/essd-11-629-2019

Bado, S., Forster, B.P., Ghanim, A.M.A., Jankowicz-Cieslak, J., Berthold, G., Luxiang, L. (2016). Protocol for measuring soil salinity. In: Protocols for Pre-Field Screening of Mutants for Salt Tolerance in Rice, Wheat and Barley. Springer, Cham, pp. 15-25. https://doi.org/10.1007/978-3-319-26590-2_3

Baldwin, A. H., & Mendelssohn, I. A. (1998). Effects of salinity and water level on coastal marshes: an experimental test of disturbance as a catalyst for vegetation change. *Aquatic Botany*, *61*(4), 255-268.

Belhadj-aissa, S., Simard, M., Ruiz, A. P., Palacios, J., & Fagherazzi, S. (2026). Mapping salt marsh hydroperiod using Synthetic Aperture Radar time series. *Remote Sensing Applications: Society and Environment*, *41*. https://doi.org/10.1016/j.rsase.2025.101850

Brodrick, P.G., Olson-Duvall, W., Ochoa, F., Jhalani, V.A. Emit-sds/SpectralUnmixing: v0.2.4 (2024), 10.5281/ZENODO.14362833

Brodrick, P.G., A.M. Chlus, U.N. Bohn, E. Greenberg, J. Montgomery, J.W. Chapman, M. Eastwood, S.R. Lundeen, R. Eckert, W. Olson-Duvall, D.R. Thompson, and R.O. Green. (2025). AVIRIS-3 L2A Orthocorrected Surface Reflectance, Facility Instrument Collection. ORNL DAAC, Oak Ridge, Tennessee, USA. https://doi.org/10.3334/ORNLDAAC/2357

Brodrick, P. G., Hestir, E. L., Slingsby, J. A., Wilson, A. M., Cardoso, A. W., Chlus, A. M., Eckert, R., Chapman, J. W., Eastwood, M., Greenberg, E., Montgomery, J., Wilder, B. A., Bohn, N., Thompson, D. R., & Green, R. O. (2026). *BioSCape: AVIRIS-NG L2 Orthocorrected Surface Reflectance* (Version 1). ORNL Distributed Active Archive Center. https://doi.org/10.3334/ORNLDAAC/2419

Byrd, K. B., O'Connell, J. L., di Tommaso, S., & Kelly, M. (2014). Evaluation of sensor types and environmental controls on mapping biomass of coastal marsh emergent vegetation. Remote Sensing of Environment, 149, 166–180. https://doi.org/10.1016/j.rse.2014.04.003

Campbell, A., Adam, E., Fatoyinbo, L., Jensen, D. J., Simard, M., Smith, K., Thakali, P., Barrenblit, A., Naidoo, L., van Deventer, H., & Stovall, A. (2025). *BioSCape Estuary Wetland Vegetation Plot Data and Habitat Extents, South Africa* (Version 1). ORNL Distributed Active Archive Center. https://doi.org/10.3334/ORNLDAAC/2441

Carpinteria Salt Marsh Reserve Management Plan (2026). University of California Natural Reserve System. Accessed at: https://csmr.nrs.ucsb.edu/management-plan/. https://doi.org/10.21973/N3X08Q

Cerubini, R., Pommerol, A., Yoldi, Z., & Thomas, N. (2022). Near-infrared reflectance spectroscopy of sublimating salty ice analogues. Implications for icy moons. *Planetary and Space Science*, *211*. https://doi.org/10.1016/j.pss.2021.105391

Convention on Wetlands (Ramsar). (1991). *Langebaan Lagoon (Ramsar Site No. 398): Ramsar Information Sheet (RIS)* (ZA398RIS). Ramsar Sites Information Service. https://rsis.ramsar.org/RISapp/files/RISrep/ZA398RIS.pdf

Das, A., Bhattacharya, B. K., Setia, R., Jayasree, G., & Sankar Das, B. (2023). A novel method for detecting soil salinity using AVIRIS-NG imaging spectroscopy and ensemble machine learning. ISPRS Journal of Photogrammetry and Remote Sensing, 200, 191–212. https://doi.org/10.1016/j.isprsjprs.2023.04.018

Day, J., Anthony, E., Costanza, R., Edmonds, D., Gunn, J., Hopkinson, C., Mann, M., Morris, J., Osland, M., Quirk, T., Rovai, A., Rybczyk, J., Spencer, T., Stephens, J., Syvitski, J., Twilley, R., Visser, J., & White, J. R. (2024). Coastal Wetlands in the Anthropocene. Annual Review of Environment and Resources, 49. https://doi.org/10.1146/annurev-environ-121922

Department of Primary Industries and Regional Development (2022). Measuring soil salinity. Government of Western Australia. Retrieved February 23, 2025, from https://www.agric.wa.gov.au/soil-salinity/measuring-soil-salinity

DWAF, 2008. The Assessment of Water Availability in the Berg Catchment (WMA 19) by Means of Water Resource Related Models: Groundwater Model Report Volume 6 – Langebaan Road and Elandsfontein Aquifer System Model. Prepared by Umvoto Africa (Pty) Ltd in association with Ninham Shand (Pty) Ltd on behalf of the Directorate : National Water Resource Planning. DWAF Report No. P WMA 19/000/00/0408.

Eckert, R., D.R. Thompson, A.M. Chlus, J.W. Chapman, M. Eastwood, M. Bernas, S. Geier, M. Helmlinger, D. Keymeulen, E. Liggett, S. Nadgauda, L.M. Rios, L.A. Shaw, W. Olson-Duvall, P.G. Brodrick, and R.O. Green. 2024. AVIRIS-3 L1B Calibrated Radiance, Facility Instrument Collection. ORNL DAAC, Oak Ridge, Tennessee, USA. https://doi.org/10.3334/ORNLDAAC/2356

FitzGerald, D. M., Fenster, M. S., Argow, B. A., & Buynevich, I. v. (2008). Coastal Impacts Due to Sea-Level Rise. Annual Review of Earth and Planetary Sciences, 36(1), 601–647. https://doi.org/10.1146/annurev.earth.35.031306.140139

Flemming, B.W. 1988. Process and pattern of sediment mixing in a microtidal coastal lagoon along the west coast of South Africa. In: De Boer, P.L., Van Gelder, A., & Nio, S.D. Tide-influenced sedimentary environments and facies. D Reidel Publ Co, Dordrecht, p. 275-288.

Forkuor, G., Hounkpatin, O. K., Welp, G., & Thiel, M. (2017). High resolution mapping of soil properties using remote sensing variables in south-western Burkina Faso: a comparison of machine learning and multiple linear regression models. *PloS one*, *12*(1), e0170478.

Gao, B-C. 1996. NDWI—A normalized difference water index for remote sensing of vegetation liquid water from space. Remote Sensing of Environment, 58(3): 257-266. https://doi.org/10.1016/S0034-4257(96)00067-3.

George K., J., & Kumar, S. (2015). Hyperspectral Remote Sensing in Characterizing Soil Salinity Severity using SVM Technique - A Case Study of Alluvial Plains. International Journal of Advanced Remote Sensing and GIS, 4(1), 1344–1360. https://doi.org/10.23953/cloud.ijarsg.122

Gopalakrishnan, T., Hasan, M. K., Haque, A. T. M. S., Jayasinghe, S. L., & Kumar, L. (2019). Sustainability of Coastal Agriculture under Climate Change. Sustainability 2019, Vol. 11, Page 7200, 11(24), 7200. https://doi.org/10.3390/SU11247200

Green, R. (2022). EMIT L2A Estimated Surface Reflectance and Uncertainty and Masks 60 m V001 [Data set]. NASA EOSDIS Land Processes Distributed Active Archive Center. Accessed 2025-02-25 from https://doi.org/10.5067/EMIT/EMITL2ARFL.001

Habibi, V., Ahmadi, H., Jafari, M., & Moeini, A. (2021). Mapping soil salinity using a combined spectral and topographical indices with artificial neural network. PLoS ONE, 16(5 May). https://doi.org/10.1371/journal.pone.0228494

Hale, W.O. & Margham, lP. 1988. Collins dictionary of biology. HarperCollins Publishers. 164. Page 178.

Hamlington, B. D., Gardner, A. S., Ivins, E., Lenaerts, J. T. M., Reager, J. T., Trossman, D. S., et al. (2020). Understanding of Contemporary Regional Sea-Level Change and the Implications for the Future. Reviews of Geophysics, 58(3), e2019RG000672. https://doi.org/10.1029/2019RG000672

Heiss, J.W. and Michael, H.A. (2014). Saltwater-freshwater mixing dynamics in a sandy beach aquifer over tidal, spring-neap, and seasonal cycles. Water Resources Research, 50(8), pp.6747-6766.

Herbert, E. R., Boon, P., Burgin, A. J., Neubauer, S. C., Franklin, R. B., Ardón, M., et al. (2015). A global perspective on wetland salinization: Ecological consequences of a growing threat to freshwater wetlands. *Ecosphere, 6*(10), 206. https://doi.org/10.1890/ES14-00534.1

Herrero, J., Castañeda, C. (2015). Two fixed ratio dilutions for soil salinity monitoring in hypersaline wetlands. PLOS ONE 10(5), e0126493. https://doi.org/10.1371/journal.pone.0126493

IPCC. (2021). Sixth Assessment Report. Retrieved from https://www.ipcc.ch/assessment-report/ar6/.

Israel, S., Vermaak, N., Andries, C., Van der Schyff, M., Tredoux, G., Jovanovic, N., Kanyerere, T., Zhang, H., Nel, J., Xu, Y. & Fourie, F. (2021). Towards sustainable exploitation of groundwater resources along the West Coast of South Africa. *Water Research Commission (WRC)*. *Report No.* 2744/1/21, Water Research Commission, Pretoria, South Africa. ISBN 978-0-6392-0271-6.

Jensen, D., Simard, M., Cavanaugh, K., Sheng, Y., Fichot, C. G., Pavelsky, T., & Twilley, R. (2019). Improving the Transferability of Suspended Solid Estimation in Wetland and Deltaic Waters with an Empirical Hyperspectral Approach. *Remote Sensing*, *11*(13), 1629. https://doi.org/10.3390/rs11131629

Jensen, D., Adams, K. H., Soloy, A., Davis, C., Belhadj-Aissa, S., Naidoo, L., Thakali, P. P., Adam, E., Barrenblitt, A., & Campbell, A. BioSCape: Coastal Wetland Soil Salinity and

Hydroperiod, California, USA, and Western Cape, South Africa. https://doi.org/10.3334/ORNLDAAC/2529

Karnieli, A., Kidron, G. J., Glaesser, C., & Ben-Dor, E. (1999). Spectral characteristics of cyanobacteria soil crust in semiarid environments. Remote Sensing of Environment, 69(1), 67–75. http://dx.doi.org/10.1016/S0034-4257(98)00110-2.

Kim, J., Grunwald, S., Rivero, R. G., & Robbins, R. (2012). Multi-scale modeling of soil series using remote sensing in a wetland ecosystem. *Soil Science Society of America Journal*, *76*(6), 2327-2341.

Kim, K.H., Heiss, J.W., Michael, H.A., Cai, W.J., Laattoe, T., Post, V.E. and Ullman, W.J., (2017). Spatial patterns of groundwater biogeochemical reactivity in an intertidal beach aquifer. Journal of Geophysical Research: Biogeosciences, 122(10), pp.2548-2562.

Kim, K.H., Michael, H.A., Field, E.K. and Ullman, W.J. (2019). Hydrologic shifts create complex transient distributions of particulate organic carbon and biogeochemical responses in beach aquifers. Journal of Geophysical Research: Biogeosciences, 124(10), pp.3024-3038.

Lafferty, K.D., Dunham, E.J., Mancini, F.T., Stewart, T.E., and Hechinger, R.F. (2017), Carpinteria Salt Marsh Habitat Polygons: U.S. Geological Survey data release, http://doi.org/10.5066/F7T72FMP.

Lamers, L. P. M., Govers, L. L., Janssen, I. C. J. M., Geurts, J. J. M., van der Welle, M. E. W., van Katwijk, M. M., van der Heid, T., Roelofs, J. G. M., & Smolders, A. J. P. (2013). Sulfide as a soil phytotoxin-a review. In *Frontiers in Plant Science* (Vol. 4, Issue JUL). Frontiers Research Foundation. https://doi.org/10.3389/fpls.2013.00268

Li, X., Liu, L., Zhao, J., & Tan, J. (2015). Optical properties of sodium chloride solution within the spectral range from 300 to 2500 nm at room temperature. *Applied Spectroscopy*, *69*(5), 635–640. https://doi.org/10.1366/14-07769R

Lorrain-Soligon, L., Robin, F., Bertin, X., Jankovic, M., Rousseau, P., Lelong, V., & Brischoux, F. (2023). Long-term trends of salinity in coastal wetlands: Effects of climate, extreme weather events, and sea water level. *Environmental Research*, *237*, 116937.

Martínez, M.L., Mendoza-González, G., Silva-Casarín, R. and Mendoza-Baldwin, E. (2014). Land use changes and sea level rise may induce a “coastal squeeze” on the coasts of Veracruz, Mexico. *Global Environmental Change*, *29*, pp.180-188.

Michael, H.A., Lubetsky, J.S. and Harvey, C.F. (2003). Characterizing submarine groundwater discharge: A seepage meter study in Waquoit Bay, Massachusetts. Geophysical Research Letters, 30(6).

Michael, H. A., Post, V. E. A., Wilson, A. M., & Werner, A. D. (2017). Science, society, and the coastal groundwater squeeze. In *Water Resources Research* (Vol. 53, Issue 4, pp. 2610–2617). Blackwell Publishing Ltd. https://doi.org/10.1002/2017WR020851

Moffett, K.B., Robinson, D.A., & Gorelick, S.M. (2010). Relationship of salt marsh vegetation zonation to spatial patterns in soil moisture, salinity, and topography. Ecosystems 13(8): 1287-1302.

Nguyen, D. N., Chiapponi, E., Nguyen, D. M., Antonellini, M., & Silvestri, S. (2024). Detection and mitigation of soil salinization risk from saline/brackish water aquaculture in coastal areas: an application of remote sensing and managed aquifer recharge. Journal of Coastal Conservation, 28(5). https://doi.org/10.1007/s11852-024-01067-w

Ochoa, F., Brodrick, P. G., Okin, G. S., Ben-Dor, E., Meyer, T., Thompson, D. R., & Green, R. O. (2025). Soil and vegetation cover estimation for global imaging spectroscopy using spectral mixture analysis. *Remote Sensing of Environment*, *324*, 114746.

Pennings, S.C. and Bertness, M.D. (1999). "Using latitudinal variation to examine effects of climate on coastal salt marsh pattern and process." Current Topics in Wetland Biogeochemistry 3: 100-111.

Qi, M., Sun, T., Zhang, H., Zhu, M., Yang, W., Shao, D. and Voinov, A. 2017. "Maintenance of salt barrens inhibited landward invasion of Spartina species in salt marshes." Ecosphere 8(10): e01982.

Rath, K. M., & Rousk, J. (2015). Salt effects on the soil microbial decomposer community and their role in organic carbon cycling: a review. *Soil Biology and Biochemistry*, *81*, 108-123.

Rhoades, J.D., Chanduvi, F., Lesch, S. (1999). Soil Salinity Assessment: Methods and Interpretation of Electrical Conductivity Measurements. FAO Irrigation and Drainage Paper No. 57. Food and Agriculture Organization of the United Nations, Rome, Italy.

U.S. Salinity Laboratory Staff, 1954. Diagnosis and Improvement of Saline and Alkali Soils. USDA Agriculture Handbook No. 60. U.S. Government Printing Office, Washington, DC.

Roberts, D. A., Gardner, M., Church, R., Ustin, S., Scheer, G., Green, R. O., & Hall, E. (1998). Mapping Chaparral in the Santa Monica Mountains Using Multiple Endmember Spectral Mixture Models. *Remote Sensing of Environment*, *65*(65), 267–279.

Savitzky, A., & Golay, M. J. E. (1964). Smoothing and Differentiation of Data by Simplified Least Squares Procedures. *Analytical Chemistry*, *36*(8), 1627–1639. https://pubs.acs.org/sharingguidelines

Shahrayini, E., & Noroozi, A. A. (2022). Modeling And Mapping of Soil Salinity And Alkalinity Using Remote Sensing Data And Topographic Factors. Environmental Modeling & Assessment, 27, 901–913. https://doi.org/10.21203/rs.3.rs-724984/v1

Silva, G. D., Roberts, D. A., Byrd, K. B., Chadwick, K. D., Walker, I. J., & King, J. Y. (2025). Using imaging spectroscopy and elevation in machine learning to estimate soil salinity in intermittently tidal wetlands. *Ecosphere*, *16*(8). https://doi.org/10.1002/ecs2.70356

Snedden, G. A., Cretini, K., & Patton, B. (2014). Inundation and salinity impacts to above- and belowground productivity in *Spartina patens* and *Spartina alterniflora* in the Mississippi River deltaic plain: Implications for using river diversions as restoration tools. Ecological Engineering, 81, 133–139. https://doi.org/10.1016/j.ecoleng.2015.04.035

Staff, U.S. Salinity Laboratory, (1954). Diagnosis and improvement of saline and alkali soils. *Agriculture handbook*, 60, US Department of Agriculture.

Sui, H., Chen, D., Yan, J., Li, B., Li, W., & Cui, B. (2022). Soil Salinity Estimation Over Coastal Wetlands Based on Random Forest Algorithm and Hydrological Connectivity Metric. *Frontiers in Marine Science*, *9*. https://doi.org/10.3389/fmars.2022.895172

Thompson, D.R, P.G. Brodrick, R.O. Green, O. Kalashnikova, S. Lundeen, G. Okin, W. Olson-Duvall, and T. Painter. (2020). EMIT L2A Algorithm: Surface Reflectance and Scene Content Masks: Theoretical Basis. Version 1.0. Jet Propulsion Laboratory, California Institute of Technology; Pasadena, California. https://earth.jpl.nasa.gov/emit/internal_resources/281

Ullman, W. J., Chang, B., Miller, D. C., & Madsen, J. A. (2003). Groundwater mixing, nutrient diagenesis, and discharges across a sandy beachface, Cape Henlopen, Delaware (USA). *Estuarine, Coastal and Shelf Science*, *57*(3), 539–552. https://doi.org/10.1016/S0272-7714(02)00398-0

Van der Linden, L.C. (2014). Salt marsh distribution and structure at Langebaan Lagoon. BSc Honours Thesis, Department of. Botany, Nelson Mandela University, South Africa. https://doi.org/10.5281/zenodo.19178320

van Deventer, H., Durand, F., & Grundling, P. (2025). Global biodiversity framework for freshwater wetlands of South Africa: Preliminary calculation of progress towards achieving the restoration target of goal 2. *Suid-Afrikaanse Tydskrif Vir Natuurwetenskap En Tegnologie*, *44*(1), 53–63. https://doi.org/10.36303/satnt.2025.44.1.1399

van Niekerk, L., Taljaard, S., Lamberth, S. J., Adams, J. B., Weerts, S. P., & MacKay, C. F. (2022). Disaggregation and assessment of estuarine pressures at the country-level to better inform management and resource protection–the South African experience. *African Journal of Aquatic Science*, *47*(2), 127–148. https://doi.org/10.2989/16085914.2022.2041388

Wang, H., Hsieh, Y.P., Harwell, M.A. and Huang, W. 2007. "Modeling soil salinity distribution along topographic gradients in tidal salt marshes in Atlantic and Gulf coastal regions." Ecological Modelling 201(3-4): 429-439.

White Jr., E., & Kaplan, D. A. (2021). Identifying the effects of chronic saltwater intrusion in coastal floodplain swamps using remote sensing. Remote Sensing of Environment, 258(December 2020), 112385. https://doi.org/10.1016/j.rse.2021.112385

Yang, J., Shen, C., Xu, T., Xie, Y., & Lu, C. (2022). On the intrusion and recovery of ocean-sourced 3H and 14C in coastal aquifers considering ocean-surge inundation. *Journal of Hydrology*, *604*. https://doi.org/10.1016/j.jhydrol.2021.127241

Yu, H., Kong, B., Wang, Q., Liu, X., & Liu, X. (2020). Hyperspectral remote sensing applications in soil: a review. *Hyperspectral remote sensing*, 269-291.

Zhu, K., Sun, Z., Zhao, F., Yang, T., Tian, Z., Lai, J., Zhu, W., & Long, B. (2021). Relating Hyperspectral Vegetation Indices with Soil Salinity at Different Depths for the Diagnosis of Winter Wheat Salt Stress. Remote Sensing, 13(2), 250. https://doi.org/10.3390/rs13020250